

# Interannual Tropospheric Aerosol Variability in the Late Twentieth Century and Its Impact on Tropical Atlantic and West African Climate by Direct and Semidirect Effects

SALIL MAHAJAN AND KATHERINE J. EVANS

*Oak Ridge National Laboratory, Oak Ridge, Tennessee*

JOHN E. TRUESDALE

*National Center for Atmospheric Research, Boulder, Colorado*

JAMES J. HACK

*Oak Ridge National Laboratory, Oak Ridge, Tennessee*

JEAN-FRANÇOIS LAMARQUE

*National Center for Atmospheric Research, Boulder, Colorado*

(Manuscript received 3 January 2012, in final form 18 May 2012)

## ABSTRACT

A new high-resolution global tropospheric aerosol dataset with monthly resolution is generated using version 4 of the Community Atmosphere Model (CAM4) coupled to a bulk aerosol model and forced with recent estimates of surface emissions for the period 1961–2000 to identify tropospheric aerosol-induced interannual climate variations. The surface emissions dataset is constructed from phase 5 of the Coupled Model Intercomparison Project (CMIP5) decadal-resolution surface emissions dataset to include reanalysis of tropospheric chemical composition [40-yr Reanalysis of Tropospheric Chemical Composition (RETRO)] wildfire monthly emissions data. A four-member ensemble run is conducted using the spectral configuration of CAM4, forced with the new tropospheric aerosol dataset and prescribed with observed sea surface temperature, sea ice, and greenhouse gases. CAM4 only simulates the direct and semidirect effects of aerosols on the climate. The simulations reveal that variations in tropospheric aerosol levels can induce significant regional climate variability on the interannual time scales. Regression analyses over tropical Atlantic and Africa suggest that increasing dust aerosols can cool the North African landmass and shift convection southward from West Africa into the Gulf of Guinea in the spring season. Further, it is found that carbonaceous aerosols emanating from the southwestern African savannas can significantly cool the region and increase the marine stratocumulus cloud cover over the southeast tropical Atlantic Ocean by aerosol-induced diabatic heating of the free troposphere above the low clouds. Experiments conducted with CAM4 coupled to a slab ocean model suggest that present-day aerosols can cool the tropical North Atlantic and shift the intertropical convergence zone southward and can reduce the ocean mixed layer temperature beneath the increased marine stratocumulus clouds in the southeastern tropical Atlantic.

## 1. Introduction

The Fourth Assessment Report (AR4) of the Intergovernmental Panel on Climate Change (IPCC) maintains that the radiative impacts of tropospheric aerosols on

Earth's climate remain among the largest sources of climate simulation errors/uncertainty owing to our limited understanding of complex interactions of aerosols within the climate system (Forster et al. 2007). A recent study estimates the total aerosol radiative forcing to be  $-1.5 \pm 0.5 \text{ W m}^{-2}$  from climate model simulations and satellite retrievals (Quaas et al. 2009). Moreover, the sign of the global precipitation response to increased tropospheric aerosols is not yet known (Denman et al. 2007). The major natural sources of tropospheric aerosols are dust and sea

---

*Corresponding author address:* Salil Mahajan, 1 Bethel Valley Road, P.O. Box 2008, Oak Ridge National Laboratory, Oak Ridge, TN 37831.  
E-mail: mahajans@ornl.gov

salt. Fossil fuel, biofuel, and biomass burning are the primary sources of major anthropogenic aerosols, which include sulfates, black carbon, and organic carbon. Wildfire emissions also form a large source of tropospheric carbonaceous and sulfate aerosols and their precursors. The contribution of anthropogenic activities to variability in wildfires and tropospheric mineral dust is poorly understood at present (e.g., Forster et al. 2007). The IPCC AR4, for example, used an estimate of 0% to 20%—with large uncertainties—for the contribution of the anthropogenic dust burden to the total dust aerosol loading in the troposphere (Forster et al. 2007).

Aerosols are primarily scatterers of solar radiation, reflecting incoming solar radiation back to space, resulting in a net negative top of the atmosphere (TOA) radiative flux. This radiative effect is referred to as the aerosol direct effect (e.g., Coakley and Cess 1985; Charlson et al. 1991). However, some aerosols absorb radiation and this direct effect can lead to both a net negative TOA radiative flux over dark surfaces, as well as a positive TOA radiative flux over reflecting surfaces such as deserts (e.g., Chylek and Wong 1995). The presence of bright low-level clouds below absorbing aerosols also results in a local positive TOA radiative flux (Haywood and Shine 1995). In addition to reduced surface solar radiative flux due to scattering, absorption of radiation by carbonaceous and mineral dust aerosols results in diabatic heating of the atmosphere. This leads to a surface radiative flux response much stronger than the TOA radiative flux response to tropospheric aerosols (e.g., Satheesh and Ramanathan 2000; Ramanathan et al. 2001).

The diabatic heating within a tropospheric column also impacts cloud formation and cloud lifetime by changing the relative humidity profile and the static stability of the column. The effect of these induced cloud changes on the radiative forcing of the Earth system is termed the “semidirect effect” (e.g., Hansen et al. 1997; Ackerman et al. 2000). The semidirect TOA radiative effect of absorbing aerosols, while typically positive, strongly depends on the vertical distribution of aerosols relative to the clouds. For example, the effect can be negative if the aerosols lie above a cloud layer, such as marine stratocumulus cloud decks found off the western coasts of continents in the subtropics (e.g., Johnson et al. 2004; Wilcox 2010). Diabatic heating of the troposphere above the boundary layer by moderately absorbing aerosols intensifies the inversion layer and reduces entrainment of air from above in the shallow clouds. The heating also results in a shallower boundary layer with a higher liquid water path of the stratocumulus clouds, which increases the reflection of shortwave fluxes back to the top of the atmosphere (e.g., Johnson et al. 2004; Sakaeda et al. 2011). Results from 15 global aerosol

models participating in the Aerosol Comparison between Models and Observations project (AeroCom) suggest that the globally averaged combined TOA radiative forcing from the direct and semidirect effect of major aerosol species is  $-0.4 \text{ W m}^{-2}$  with as large an uncertainty (Forster et al. 2007).

Further, microphysical interactions of aerosols with clouds can indirectly affect the climate system. The indirect effects of aerosols, primarily through the cloud albedo effect (Twomey effect) and the cloud lifetime effect (Albrecht effect) (Twomey 1977; Albrecht 1989; Rosenfeld 2000), are among the largest sources of uncertainty in climate simulations due to poor understanding and simulation of microphysically induced aerosol–cloud interactions (Forster et al. 2007). Models that include all major aerosol species estimate the radiative forcing from each of these two indirect effects ranges from  $-0.3$  to  $-1.8 \text{ W m}^{-2}$  (Forster et al. 2007; Denman et al. 2007).

Most observational or modeling studies of aerosol impacts on the climate system attempt to quantify and constrain the uncertainty of direct or indirect radiative forcings with respect to the present aerosol conditions. However, only a few studies (e.g., Huang et al. 2009a; Mahowald et al. 2010) focus on the impact of the interannual variability of aerosols on the climate system. Studies of aerosol induced trends in the past century also focus on the long-term changes (e.g., Ramanathan et al. 2005) with little analysis of aerosol-induced interannual variations. Phase 5 of the Coupled Model Intercomparison Project (CMIP5) production simulations for the Fifth Assessment Report (AR5) of the IPCC will be forced with decadal resolution of aerosol precursor emissions to capture aerosol-forced trends over the last century (Lamarque et al. 2010). These simulations will therefore not resolve the aerosol-induced interannual climate variability.

The focus of this study is to identify and understand tropospheric aerosol-induced interannual variations of global and regional climate by direct and semidirect effects from simulations of the spectral configuration of Community Atmosphere Model version 4 (CAM4), which is the atmospheric component of the Community Earth System Model version 1.0 (CESM1.0). For this purpose, we have generated a new estimate of global atmospheric aerosol distribution to force CAM4 with a more realistic time-varying, high-resolution, aerosol-induced radiative forcing. The global tropospheric aerosol distribution dataset is generated from a new emissions dataset, which is derived from the CMIP5 surface emissions dataset by enhancing it to include monthly surface wildfire emissions data for the period 1961–2000, lending interannual variability to aerosols radiative forcing.

Aerosols have been found to play a particularly important role in the climate of the tropical Atlantic and West Africa (e.g., Prospero and Lamb 2003; Yoshioka et al. 2007; Huang et al. 2009a; Sakaeda et al. 2011), the Amazon basin (e.g., Koren et al. 2004; Pöschl et al. 2010), and Southeast Asia (e.g., Ramanathan et al. 2001, 2005; Chung and Ramanathan 2006; Lau et al. 2006; Collier and Zhang 2009). In this study, we focus on the impact of variability in aerosols on the climate of the tropical Atlantic and West Africa. The tropical Atlantic and the African continent bear an influx of different aerosol species over different latitudinal bands throughout the year (e.g., Kaufman et al. 2005; Huang et al. 2009a). Sulfate aerosols are advected to the north tropical Atlantic from emissions in North America and Europe. Dust emitted from the Sahara desert and the Sahel region travels westward across the tropical North Atlantic between 5° and 30°N, peaking in the boreal summer (e.g., Prospero and Carlson 1972; Huang et al. 2009b). Biomass burning and forest fires over the Sahel region and central Africa result in carbonaceous aerosols over central Africa and the equatorial and south tropical Atlantic Ocean from July to September (e.g., Haywood et al. 2003, 2004; Matichuk et al. 2007). Observational and modeling studies reveal that increased aerosols over tropical Africa and tropical Atlantic tend to reduce the West African rainfall as well as cloud amount (e.g., Huang et al. 2009a). Increased aerosols are also associated with increased shallow cloud cover over the north and south tropical Atlantic off the west coast of Africa (e.g., Kaufman et al. 2005).

In the following section, we describe the methodology of generating the new monthly high-resolution global tropospheric aerosol dataset from surface emissions. We briefly describe our experiments with CAM4 forced with the new aerosol dataset in section 3. In section 4, we present a comparison of the simulated aerosol distribution with Moderate Resolution Imaging Spectroradiometer (MODIS) satellite retrievals, and we discuss the trends and variability related to the new aerosol distribution dataset in section 5. In section 6, we briefly discuss aerosol-induced variability on the global radiative forcing in the context of our simulations. We focus on the direct and semidirect effects of aerosols on tropical Atlantic and the African continents—regions with large mean aerosol loadings and exhibiting large aerosol variability—in section 7. We present our results from simulations of CAM4 coupled with a slab ocean model (SOM) to assess the role of thermodynamic feedbacks in the response of tropical Atlantic and Africa to aerosol forcing in section 8. Finally, we summarize and discuss our results in section 9.

## 2. Generating tropospheric aerosol dataset from surface emissions data

A realistic three-dimensional tropospheric aerosol monthly dataset for the latter part of the twentieth century is created using the finite volume dynamical core of CAM4 at a horizontal resolution of  $0.9^\circ \times 1.25^\circ$ , coupled to a bulk aerosol model (BAM). The dataset includes the tropospheric distribution of five major anthropogenic and natural aerosol species, namely sulfates, black carbon, organic carbon, sea salt, and dust. BAM only computes the bulk mass of aerosols and assumes a lognormal size distribution for all aerosols, and includes sulfur chemistry (Lamarque et al. 2005; Emmons et al. 2010; Tie et al. 2001, 2005). CAM4 simulates the direct and semidirect effects of aerosols and excludes the indirect effects. The CAM4-BAM model setup is prescribed with observed sea surface temperature (SST) and sea ice extent as the lower boundary conditions. The model setup is forced with a time series of surface emissions of black carbon, organic carbon, and sulfate aerosols. Further, the time series of sulfate aerosol precursors (sulfur dioxide and dimethyl sulfide) and oxidants (ozone, hydroxyl radical, nitrates, and hydrogen peroxide) are prescribed. The model incorporates dust (Mahowald et al. 2006b; Zender et al. 2003) and sea salt (Mahowald et al. 2006a) aerosols and simulates their entrainment in the atmosphere based on surface conditions. The deposition fluxes of the different aerosol species are also computed by the model. The finite volume discretization is better suited for climate simulations that include atmospheric chemistry and tracer transport than the spectral configuration, because mass is conserved in the finite volume discretization.

The CAM4-BAM model setup allows for explicitly interactive sulfur chemistry within the GCM, generating a consistent chemistry–climate simulation (albeit with systematic CAM4 model biases; R. Neale et al. 2011, unpublished manuscript). The transport of aerosol precursors, oxidants, derived sulfate, and other aerosol species is driven by CAM4-generated atmospheric flow online. Our goal here is to generate a realistic 3D distribution of major aerosol species from a simulation that includes the feedbacks between aerosols and the model climate. The radiative forcing of aerosols is computed online, allowing the climate system to respond to the forcing, which would in turn also affect the transport of aerosols and their precursors. Typically, chemistry transport models generate atmospheric tracer distributions offline, driven by observations or reanalyses products, which do not capture complex interactions between chemistry and climate.

The emissions dataset generated for the CAM4-BAM model were derived from the emissions data created for the CMIP5 model simulations (Lamarque et al. 2010). The CMIP5 emissions dataset has been created at a resolution of  $0.5^\circ \times 0.5^\circ$  at decadal increments for the period 1850–2000 from 40 regions worldwide and 12 activity sectors that release emissions (Lamarque et al. 2010). The purpose of CMIP5 emissions dataset was to provide data for all emission species that are important for the generation of ozone and aerosols in global atmospheric chemistry models. For a large number of species required in complex chemistry models, the global and regional data inventories are limited temporally and show large differences among them for uncontrolled emissions such as biomass burning (Kasischke and Penner 2004). Since the central focus of CMIP5 is on long-term trends, emissions were only provided every decade, with a seasonal cycle of biomass burning emissions only (Lamarque et al. 2010).

However, data at monthly resolution are available for the latter part of the twentieth century for key aerosol species such as sulfur dioxide (Smith et al. 2011) and carbonaceous aerosols (Bond et al. 2004; Junker and Liousse 2008) and are sufficient for the relatively simple chemistry module of BAM. Here, we exploit the 40-yr Reanalysis of Tropospheric Chemical Composition (RETRO) wildland fire inventory (Schultz et al. 2008) from 1961 to 2000, which includes emissions of black carbon, organic carbon, sulfur dioxide, and sulfates among several trace compounds from wildfires. The RETRO inventory is available at a spatial resolution of  $0.5^\circ \times 0.5^\circ$  at monthly intervals. The inventory is based on an extensive literature review of existing datasets, satellite-derived estimates, and a semiphysical numerical model to simulate fire occurrence and spread (Schultz et al. 2008).

We combine RETRO data with the CMIP5 anthropogenic emissions to generate an emissions dataset with monthly variability, by replacing the wildfire component of CMIP5 emissions data of black carbon, organic carbon, sulfur dioxide, and sulfates with that from RETRO data for the period 1961–2000. While the RETRO data contain monthly resolutions of several anthropogenic emissions as well, they lack data for anthropogenic tracer species of black and organic carbon. In lieu of comprehensive monthly data for these species we opted to use the AR5 anthropogenic inventories and simply interpolate decadal averaged values to monthly resolution. The new emissions dataset, which we call the CMIP5-RETRO, includes both the long-term trend from anthropogenic emissions and interannual variability and trends induced by wildfires for the period 1961–2000. The CMIP5-RETRO emissions data, regridded to  $0.9^\circ \times 1.25^\circ$  resolution to match

CAM4 resolution, is then used to force the CAM4-BAM model setup to generate a time-dependent tropospheric distribution of aerosols at monthly temporal resolution and a horizontal spatial resolution of  $0.9^\circ \times 1.25^\circ$  for the period 1961–2000. We refer to it as the CMIP5-RETRO *aerosol* dataset.

We also generate a climatology of preindustrial tropospheric aerosol distribution from a 10-yr simulation using the above CAM4-BAM model setup, but forced with the best estimates of a monthly climatology of surface emissions in the preindustrial era (Lamarque et al. 2010).

### 3. Model setup for aerosol-forced twentieth-century simulations

We use the spectral configuration of CAM4 (Neale et al. 2010) with a T85 spectral truncation (K. Evans et al. 2012, unpublished manuscript) for simulating the direct and semidirect radiative effects of aerosols. The T85 spectral truncation of spectral CAM4 is similar to the finite volume dynamical core's  $1^\circ$  horizontal resolution based on the kinetic energy spectra equivalent resolution analysis (Williamson 2008). CAM4 exists as the atmospheric component of the Community Climate System Model version 4 (CCSM4.0) and is also supported as an atmospheric component in the more recent Community Earth System Model version 1.0. In our experiments, CAM4 is coupled to the Community Land Model version 4.0 (CLM4) and observed surface oceanic and sea ice conditions (Rayner et al. 2006) are prescribed as the lower boundary conditions.

CAM4 allows for a time-dependent and geographically varying tropospheric distribution of the five major anthropogenic and natural aerosol species as listed in the previous section (Neale et al. 2010). We exploit this capability in our experiments to understand regional climate variability induced by aerosols. As mentioned earlier, aerosols and cloud microphysics are uncoupled in CAM4, permitting direct and semidirect radiative effects of different aerosol species but excluding indirect effects of aerosols such as aerosol activation, aerosol–cloud feedback, etc. Also, secondary organic aerosols are not included in CAM4. While these exclusions limit the completeness of the simulation, they allow us to clearly isolate the impacts of the direct and semidirect effects of aerosols on the climate system from our experiments.

Sulfates and sea salt aerosol species in the troposphere predominantly scatter incoming solar radiation, whereas dust and carbonaceous aerosols are strongly absorbing in the visible wavelengths and lead to an increase in the shortwave diabatic heating of the troposphere in CAM4. The specific extinction, single scattering albedo, and the

asymmetry parameter of each of the aerosol species is prescribed for the spectral solar insolation and the column integrated values such as the aerosol optical depth are diagnostically computed. Further, sulfates, sea salt, and hydrophilic organic carbon are subjected to hygroscopic growth in the model, which changes the optical properties of these aerosol species based on the relative humidity profile in the tropospheric column at each radiative time step (Neale et al. 2010). The radiative forcing from the aerosols is diagnostically computed from the aerosols in the atmospheric column in CAM4. By prescribing the aerosols in CAM4, we remove the feedback mechanisms between the aerosols and the climate system and focus on the response of the climate system to aerosol-induced radiative forcing.

We run two different sets of four-member ensemble runs with the spectral configuration of T85 CAM4 for the period 1961–2000. Both experimental sets are forced with the observed SST and sea ice boundary conditions and volcanic aerosols for the simulated period. The first set is forced with 1961–2000 tropospheric CMIP5 + RETRO aerosol dataset as derived above from CMIP5 + RETRO emissions (section 2) and is called the AMIP-CMIP5AERO + RETRO set, whereas the second set is forced with the preindustrial climatology of tropospheric aerosol distribution and is called the AMIP-1850AERO set. Each of the ensemble member runs in each set are started with different initial conditions of the atmosphere.

#### 4. Comparison of model-derived aerosol dataset with MODIS data

Figure 1a shows the ensemble averaged total aerosol optical depth for the boreal spring season of the AMIP-CMIP5AERO + RETRO simulations averaged over the period 1991–2000. Figure 1b shows an estimate of the boreal spring total aerosol optical depth from the MODIS instrument on the *Terra* satellite averaged over the period 2001–10. Figure 1c shows the difference between the two. The details of MODIS retrieval algorithms and validation of aerosol products can be found in Remer et al. (2005). The MODIS instrument can reasonably measure total aerosol optical depth over the oceans, but retrievals over bright land surfaces are difficult. CAM4 seems to be overestimating the total aerosol optical depth over the north tropical Atlantic ocean and underestimating it over the south tropical Atlantic/Africa, the Indian subcontinent, Southeast Asia, and East Asia.

Dust and sulfate are the dominant species of aerosols in the north tropical Atlantic Ocean, suggesting that CAM4 is overestimating dust and sulfate aerosols over

the north tropical Atlantic. Other global aerosol models participating in the AeroCom project also overestimate the dust aerosol optical depth off West Africa (Huneeus et al. 2011). The negative biases in aerosol optical depth can largely be attributed to underestimations of carbonaceous aerosols. Again, other AeroCom global aerosol models also underestimate carbonaceous aerosol optical depth over these regions—for example, by a factor of 0.6 over the south equatorial African region (Koch et al. 2009). A significant positive trend is observed in carbonaceous aerosols over the latter part of the twentieth century, and hence a part of the lower estimate of carbonaceous aerosols by CAM4 could be attributed to the use of different periods of data for CAM4 simulations (1991–2000) and MODIS estimates (2001–10) to compute the difference between the two datasets. It should also be noted that while model simulations of aerosol optical depth suffer from uncertainty arising from uncertainty in emissions, aerosol process parameterization, and so on, MODIS retrievals also suffer from severe biases; for example, cloud contamination in retrievals could lead to an overestimation of aerosol optical depth by 10%–15% (e.g., Kaufman et al. 2005; Yu et al. 2006).

#### 5. Trends and variability in aerosol distribution

Figure 2a shows the time series of the ensemble average of globally and annually averaged total aerosol optical depth in the visible range from AMIP-CMIP5AERO + RETRO experiment set for the period 1961–2000. Figures 2b–f show the time series of the contribution of individual aerosol species to the total optical depth. The dashed lines in Fig. 2 indicate the spread among the four ensemble members represented as two standard deviations from the mean. The spread among the ensemble members with the same prescribed aerosol distribution dataset results from the varied hygroscopic growth of aerosols in each run, which is computed diagnostically in the model and is dependent upon the relative humidity profile in the atmospheric column. A linear fit to the time series is also shown in Fig. 2, indicating trends in different aerosol species. The trends in the total aerosol optical depth and contributions from sulfate, black carbon, and organic carbon to the optical depth are each statistically significant at the 95% confidence level based on a two-tailed *t* test. The sulfate aerosols peak in the eighties and have been declining thereafter, reflecting the regulations to reduce sulfur emissions in the Western Hemisphere in the 1980s (e.g., Smith et al. 2001). The optical depths of black carbon and organic carbon, however, have been monotonically increasing since the 1960s. Mahowald et al. (2010), using paleoproxy data, estimate a doubling

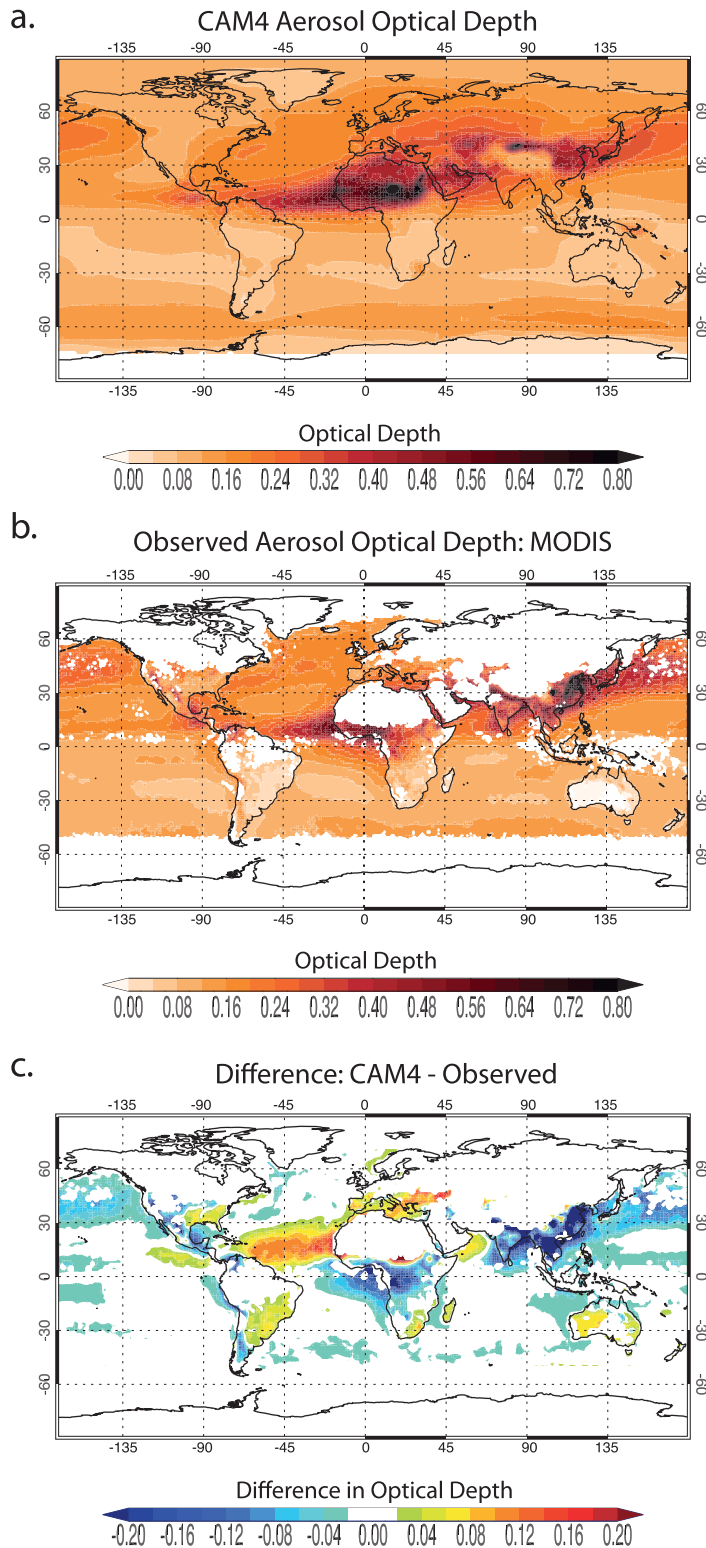


FIG. 1. Comparison of CAM4-simulated aerosol optical depth with MODIS estimate. (a) Ensemble averaged total aerosol optical depth averaged over the period 1991–2000 of the AMIP-CMIP5AERO + RETRO simulations for the boreal spring season, (b) estimate of the total aerosol optical depth from MODIS instrument on the *Terra* satellite at 500 nm averaged over the period 2001–10 for the boreal spring season, and (c) the difference between the model simulation and MODIS estimate.

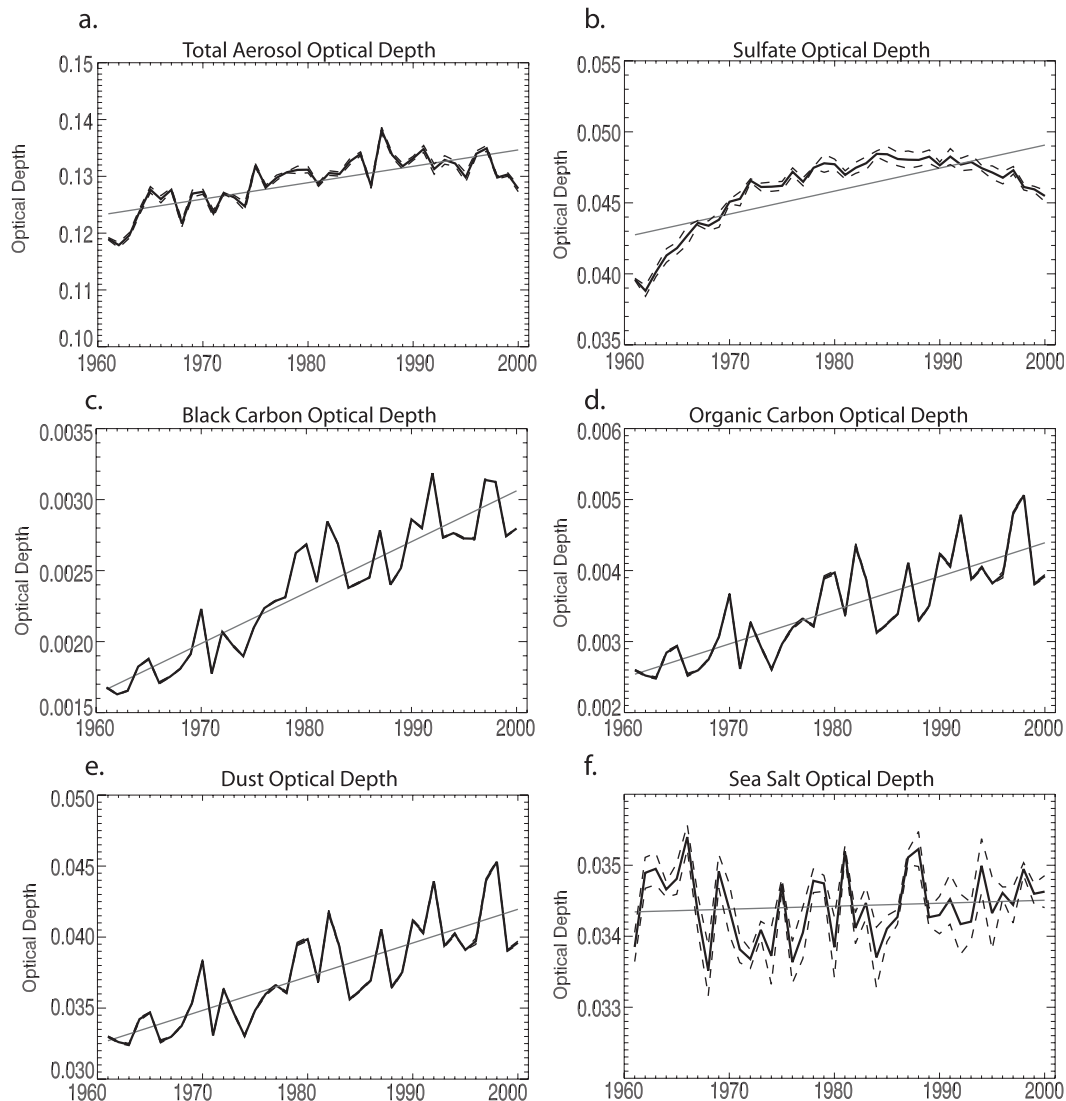


FIG. 2. Aerosol optical depth time series. Time series of ensemble averaged globally and annually averaged tropospheric optical depth of (a) all, (b) sulfate, (c) black carbon, (d) organic carbon, (e) dust, and (f) sea salt aerosols for the time period 1961–2000 of the AMIP-CMIP5AERO + RETRO simulations. The solid black lines show the ensemble averaged mean and the dashed lines show the one standard deviation of the mean estimate. The gray line represents a linear fit to the time series.

of desert dust in the twentieth century. While CAM4-BAM does not capture the increasing trend in dust aerosol optical depth in the latter part of the twentieth century, a peak in dust optical depth is noted in the 1980s similar to Mahowald et al. (2010).

Figure 3 shows the spatial pattern of the trends in the ensemble average of annually averaged total optical depth and for each of the aerosol species in the troposphere. Statistically significant increasing trends in the sulfate aerosol optical depth are seen over Southeast Asia, North Africa, and off the west coast of Mexico, with declining trends over eastern North America and

Europe. Black carbon and organic carbon also show strong positive trends over Southeast Asia, central Africa, Mexico, and central South America, with declining trends over Europe. A positive trend in dust optical depth is seen over the Sahel region similar to observations (Mahowald et al. 2010). Both positive and negative trends are observed in the sea salt aerosol optical depth over tropical oceans and are probably caused by changes in surface winds. The trend in aerosol distribution is noted throughout the troposphere. Figure 4 shows the change in the zonal mean vertical profile of sulfate, black carbon, organic carbon, and dust aerosols between

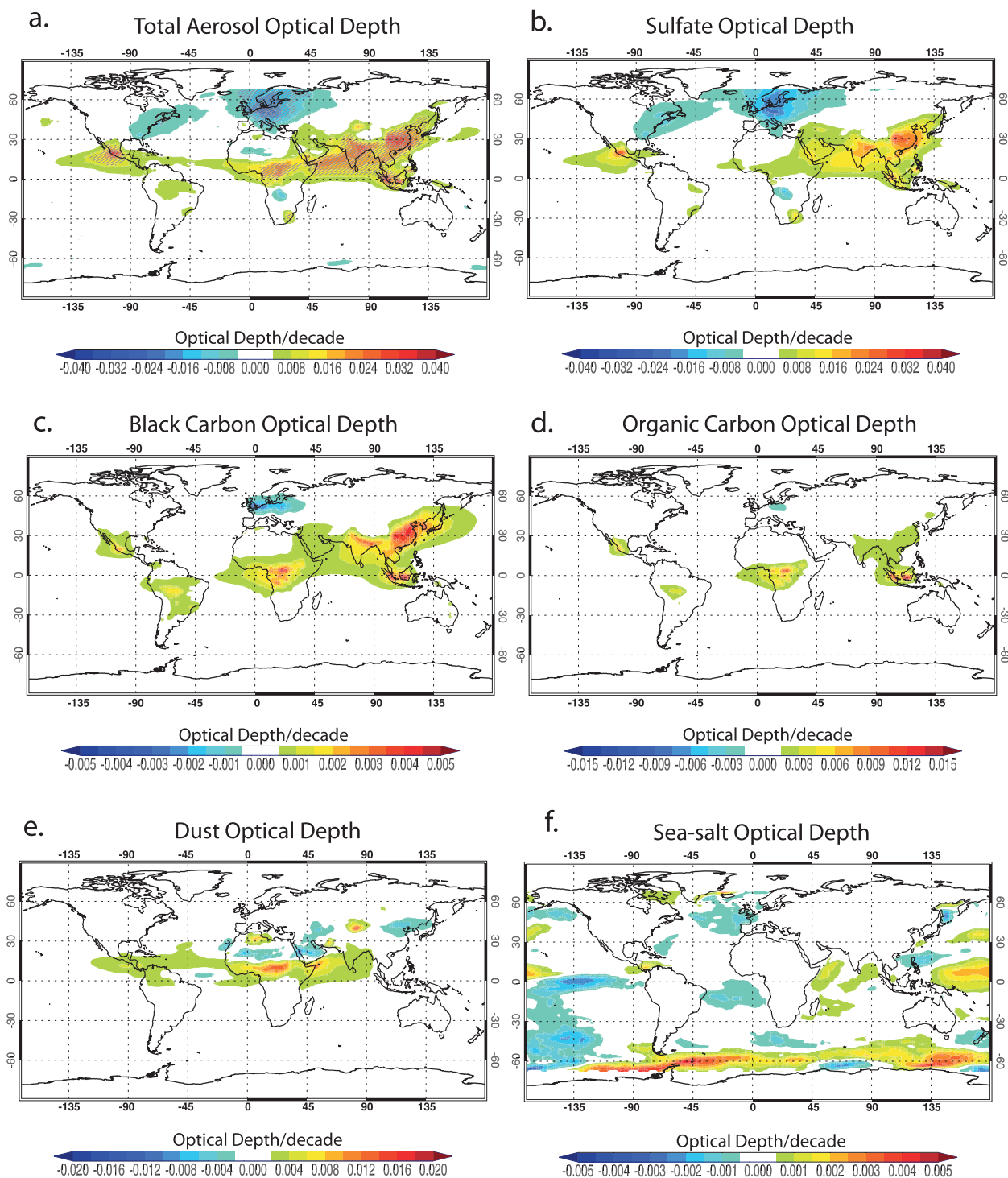


FIG. 3. Spatial trends of aerosol optical depth. Linear trends of ensemble averaged annual mean tropospheric optical depth of (a) all, (b) sulfate, (c) black carbon, (d) organic carbon, (e) dust, and (f) sea salt aerosols for the period 1961–2000 of the AMIP-CMIP5AERO + RETRO simulations. The hatching in (a) indicates regions where the trends in total aerosol optical depth is statistically significant at the 95% confidence level based on a two-tailed  $t$  test.

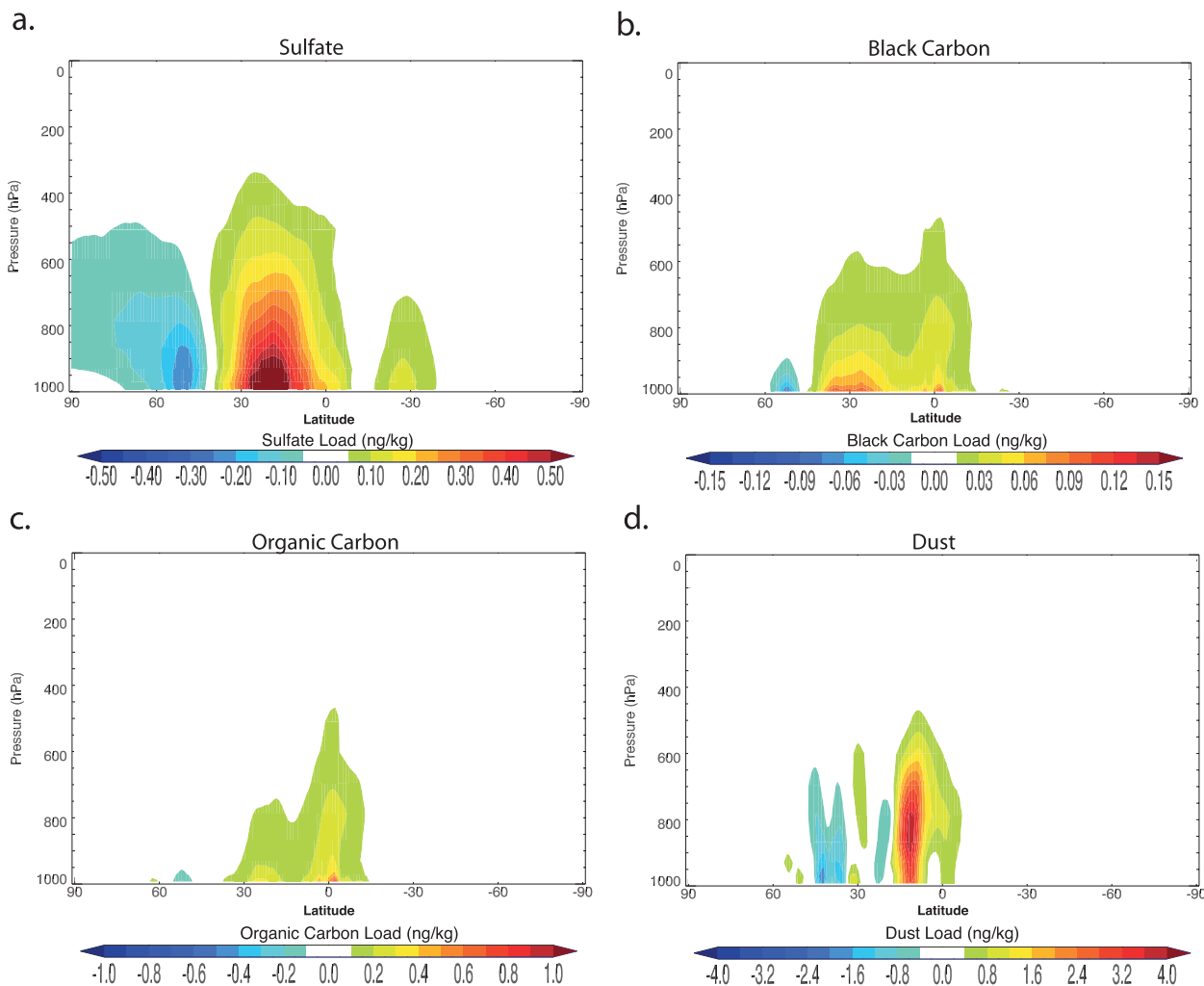


FIG. 4. Change in vertical profile of zonally averaged aerosols from 1960s to 1990s. Difference (1990s – 1960s) in the zonally averaged annual mean aerosol loading of (a) sulfate, (b) black carbon, (c) organic carbon, and (d) dust between the 1991–2000 and the 1961–70 periods.

the 1990s and the 1960s. The increase in sulfate and carbonaceous aerosols is clearly seen in the tropical regions throughout the lower and middle troposphere along with a decline in sulfate aerosols in the midlatitudes. An increase in dust aerosol is also noted in the tropical troposphere. The change in vertical distribution of absorbing aerosols can significantly alter the vertical thermal structure of the troposphere by the semidirect effect and affect clouds, as discussed in the introduction.

The interannual variability of the aerosol distribution arising from the new aerosol tropospheric dataset is clearly noted in the time series plot of AMIP-CMIP5AERO + RETRO runs (Fig. 2). Figure 5 shows the interannual standard deviation of linearly detrended total optical depth and that of individual aerosol species for the ensemble average of the AMIP-CMIP5AERO + RETRO experiment set. The strongest interannual variability of

total aerosol optical depth is seen over Southeast Asia, the Arabian Sea, central and North Africa, and central South America (Fig. 5a). Most of the interannual variability in North America and central Europe can be attributed to variations in sulfate aerosol optical depth (Fig. 5b). The linear detrending procedure is not able to completely remove the variability associated with the rise of anthropogenic sulfate aerosols until the eighties and the decline thereafter, and some of this variability shows up as interannual variability in Fig. 5b. However, interannual variability of sulfate along with carbonaceous aerosols over central Africa, Southeast Asia (particularly over Indonesia), central South America, and Mexico can be attributed to variability in wildfire emissions (Figs. 5b–d). Emissions from these land sources also drive the variability of carbonaceous aerosols over the adjacent tropical oceans, particularly over the tropical

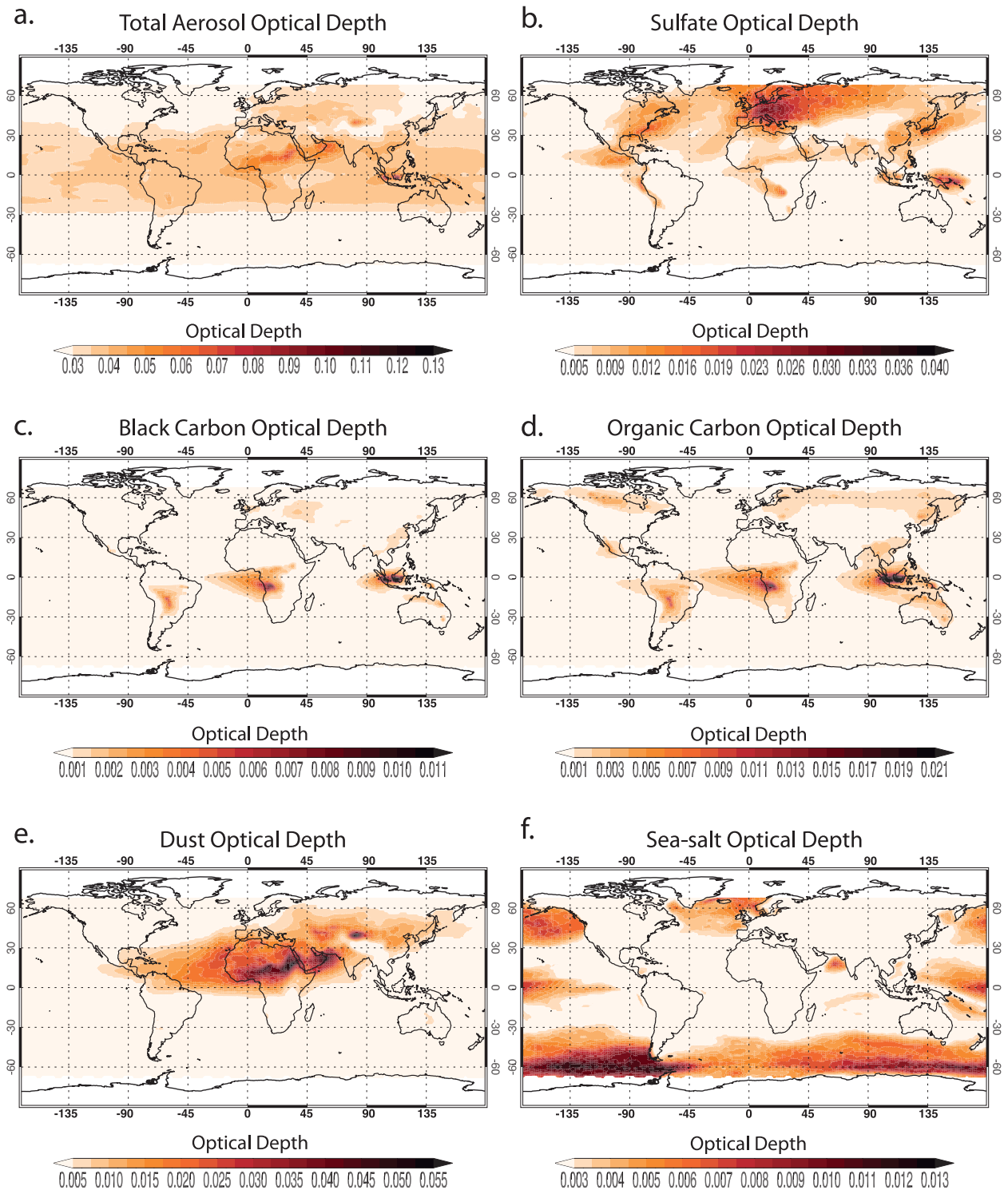


FIG. 5. Interannual variability of aerosol optical depth. Standard deviation of detrended ensemble averaged annual mean tropospheric optical depth of (a) all, (b) sulfate, (c) black carbon, (d) organic carbon, (e) dust, and (f) sea salt aerosols for the period 1961–2000 of the AMIP-CMIP5AERO + RETRO simulations.

Atlantic and tropical Indian Oceans (Figs. 5c,d). The strongest variability in dust optical depth is seen over the Sahara desert, the Sahel region, Middle East Asia, and west and central Asia (Fig. 5e). The variability in dust in these regions also drives the variability of dust optical depth over the tropical North Atlantic Ocean, the Arabian Sea, and the western parts of the North Pacific Ocean (Fig. 5e). Sea salt optical depth interannual variability is the strongest over the extratropical oceans, with some variability is also exhibited over the central tropical Pacific Ocean and the Arabian Sea (Fig. 5f).

## 6. Aerosol-induced variability in radiative forcing

The interannual variability of aerosol distribution induces increased interannual variability in the radiative forcing of the climate system in AMIP-CMIP5AERO + RETRO experiment (forced with the new CMIP5 + RETRO aerosol dataset) as compared to the AMIP-1850AERO experiment set (forced with preindustrial aerosol climatology in all seasons). Figure 6 shows the difference in the interannual standard deviation of clear-sky shortwave radiation flux at the surface between the ensemble average of AMIP-CMIP5AERO + RETRO and AMIP-1850AERO experiment sets for the boreal spring and summer seasons. The clear-sky shortwave surface radiative flux is an indicator of the direct aerosol radiative forcing on the climate system. Only regions with statistically significant differences at the 95% confidence level based on a one-tailed  $F$  test of ratio of variances are shaded in Fig. 6. Differencing the interannual variability in the AMIP-1850AERO experiment set from the AMIP-CMIP5AERO + RETRO removes the component of the variability induced by greenhouse gas and SST forcings, as the same forcings are prescribed in the two simulation sets. The residual interannual variability can thus be attributed to the variability in aerosols.

The spatial pattern of the induced variability in clear-sky shortwave radiative flux in spring is similar to the spatial pattern of the aerosol optical depth in spring, as expected, with the largest variability seen over central Africa, Southeast Asia, Europe, and central Asia (Fig. 6a). Similarly, the largest variability in the summer is seen over Middle East Asia, the Arabian Sea, northeastern Africa, central Asia, southwest equatorial Africa, and the southeastern tropical Atlantic. Over central South America and Indonesia, statistically significant differences are observed in the boreal fall season (not shown), when the variability in carbonaceous aerosol optical depth is the strongest there.

To test the impact of the difference in the mean aerosol distribution between AMIP-CMIP5AERO + RETRO and AMIP-1850AERO with regard to the simulated difference in radiative forcing variability, we

conducted two more CAM4 experiments with prescribed climatology of SST and sea ice conditions as the lower boundary conditions. The first experiment was forced with a climatology of global tropospheric aerosols computed from the CMIP5 + RETRO dataset from the period 1981–2000, and the second experiment was forced with a climatology of preindustrial aerosol distribution. Differences in the interannual variability noted between the two runs in clear-sky shortwave surface radiation flux are not statistically significant. These results indicate that the interannual variability differences seen in AMIP-CMIP5AERO + RETRO and AMIP-1850AERO experiment sets are largely induced not by the greater amount of aerosols, but by the interannual variability in the CMIP5 + RETRO aerosol dataset.

We also conducted an ensemble run similar to the AMIP-CMIP5AERO + RETRO experiment, but prescribed with CMIP5 decadal aerosol dataset derived from CMIP5 decadal emissions dataset (Lamarque et al. 2010). The trends in the globally averaged aerosol optical thickness in this experiment are similar to those in the AMIP-CMIP5AERO + RETRO experiment with the mean differing by only about 10%. The difference in the radiative forcing variability between this ensemble and the AMIP-CMIP5AERO + RETRO ensemble (not shown) is similar to that between AMIP-CMIP5AERO + RETRO and AMIP-1850AERO, as seen in Fig. 6. Again, this suggests that the interannual radiative forcing variability induced in AMIP-CMIP5AERO + RETRO is primarily caused by the interannual variability of CMIP5 + RETRO aerosol dataset.

The largest aerosol variability of dust and carbonaceous aerosols is seen over North Africa, central Africa, and the north tropical Atlantic. However, the difference in the standard deviation of land surface temperature, precipitation, and clouds (not shown) in these regions between the AMIP-CMIP5AERO + RETRO and AMIP-1850AERO experiments is not statistically significant and seems to be within the natural and greenhouse gas-induced variability of the model climate system (Fig. 6). In the following section, we focus on extracting the climate response to aerosol variability in these regions by conducting regression analyses. In the future, we plan to conduct a detailed analysis of aerosol-induced climate variability over other regions of the world.

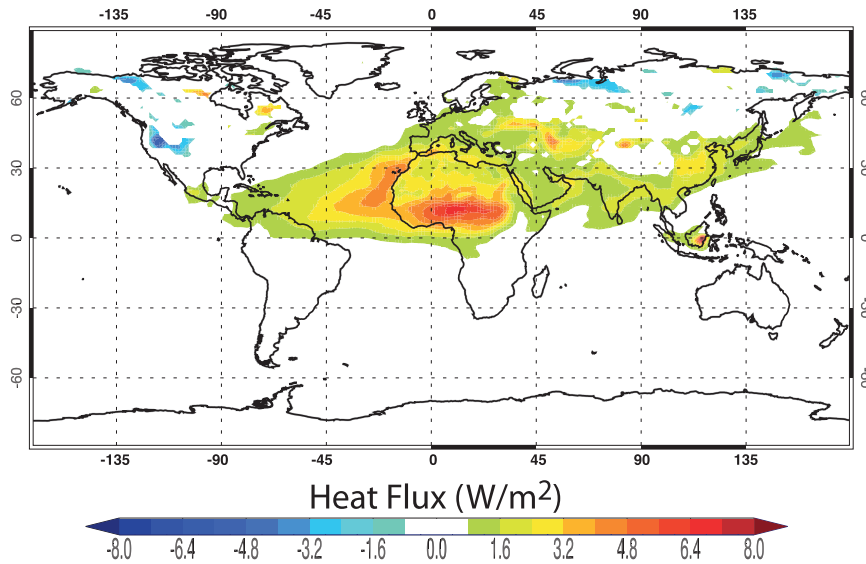
## 7. Aerosol-induced climate variability over West Africa and the tropical Atlantic Ocean

### a. Dust aerosol-induced climate variability

The strongest variability of dust optical depth over North Africa and the north tropical Atlantic is observed

a.

## Clear-sky Shortwave Radiative Flux: Spring



b.

## Clear-sky Shortwave Radiative Flux: Summer

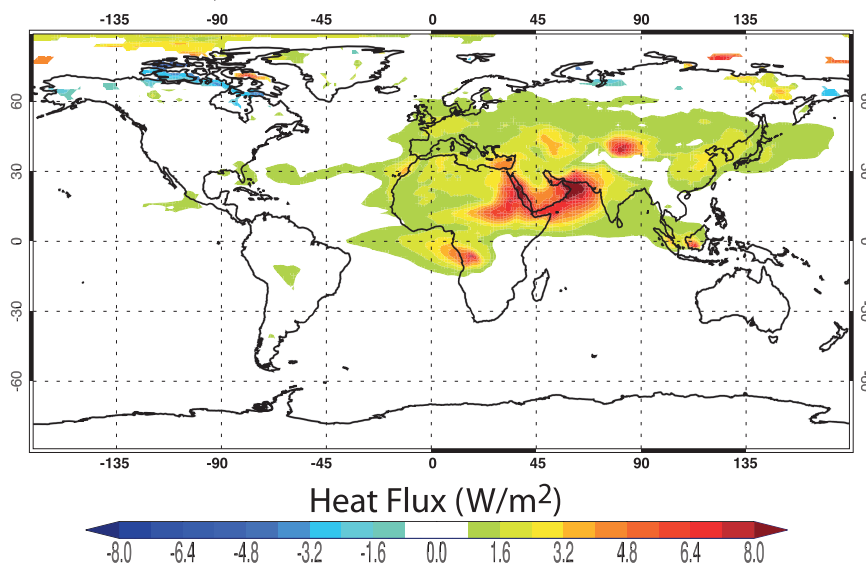


FIG. 6. Aerosol-induced variability. Difference in standard deviation (AMIP-CMIP5AERO + RETRO – AMIP-1850AERO) of clear-sky shortwave surface radiative flux ( $\text{W m}^{-2}$ ) for the (a) boreal spring season and (b) boreal summer season between AMIP-CMIP5AERO + RETRO and AMIP-1850AERO experiment sets. Only regions where the difference in variance between the two experiment sets is statistically significant at the 95% confidence level based on a one-tailed  $F$  test of ratio of variances are shaded.

in the boreal spring season in the AMIP-CMIP5AERO + RETRO experiment, similar to that in the observations (Huang et al. 2009b). This variability is reflected in the net radiative forcing at the top of the model (TOM) there in the ensemble average. Figure 7a shows a regression of the net TOM radiative flux over the North African and tropical North Atlantic region in the spring season (March–May averaged) on a dust aerosol optical depth index for the ensemble. The dust index is defined as the regionally averaged dust optical depth over tropical North Africa ( $5^{\circ}$ – $20^{\circ}$ N,  $10^{\circ}$ W– $30^{\circ}$ E) in the spring season.

Over the tropical Atlantic Ocean and West Africa, an increase in dust aerosols is associated with an increase in the net outgoing radiation at the TOM, indicating a negative TOA radiative forcing associated with dust aerosols. The increase in TOM radiative flux is largely due to the increase in the reflection of shortwave radiation both by dust aerosol particles (direct effect) and increased shallow clouds (semidirect effect), as discussed later in the section. A regression of the clear-sky TOM shortwave flux against the dust index clearly indicates the increased scattering of shortwave radiation back to space (not shown). On the other hand, over the bright desert surfaces of the Sahel in central North Africa, the absorbing dust aerosols reduce the amount of available shortwave radiation that is reflected by the surface and are associated with a positive radiative TOA forcing. A regression of the clear-sky TOM shortwave radiation flux against the dust aerosol index again confirms this direct effect of dust aerosols over the region (not shown).

At the surface, dust aerosols are associated with a net negative radiative forcing. The net surface radiative forcing is several times larger than the net TOM radiative forcing over tropical West Africa and even opposite in sign over central tropical North Africa. This difference is again caused by the absorption of shortwave radiation by dust aerosols that warms up the atmosphere and allows less shortwave radiation to reach the surface in CAM4. This effect is seen as an upward flux of shortwave radiation from the surface to the atmosphere in Fig. 7c. The upward flux of surface shortwave radiation is compensated by the reduced upward fluxes of longwave radiation, surface sensible heat, and surface latent heat (Figs. 7d–f).

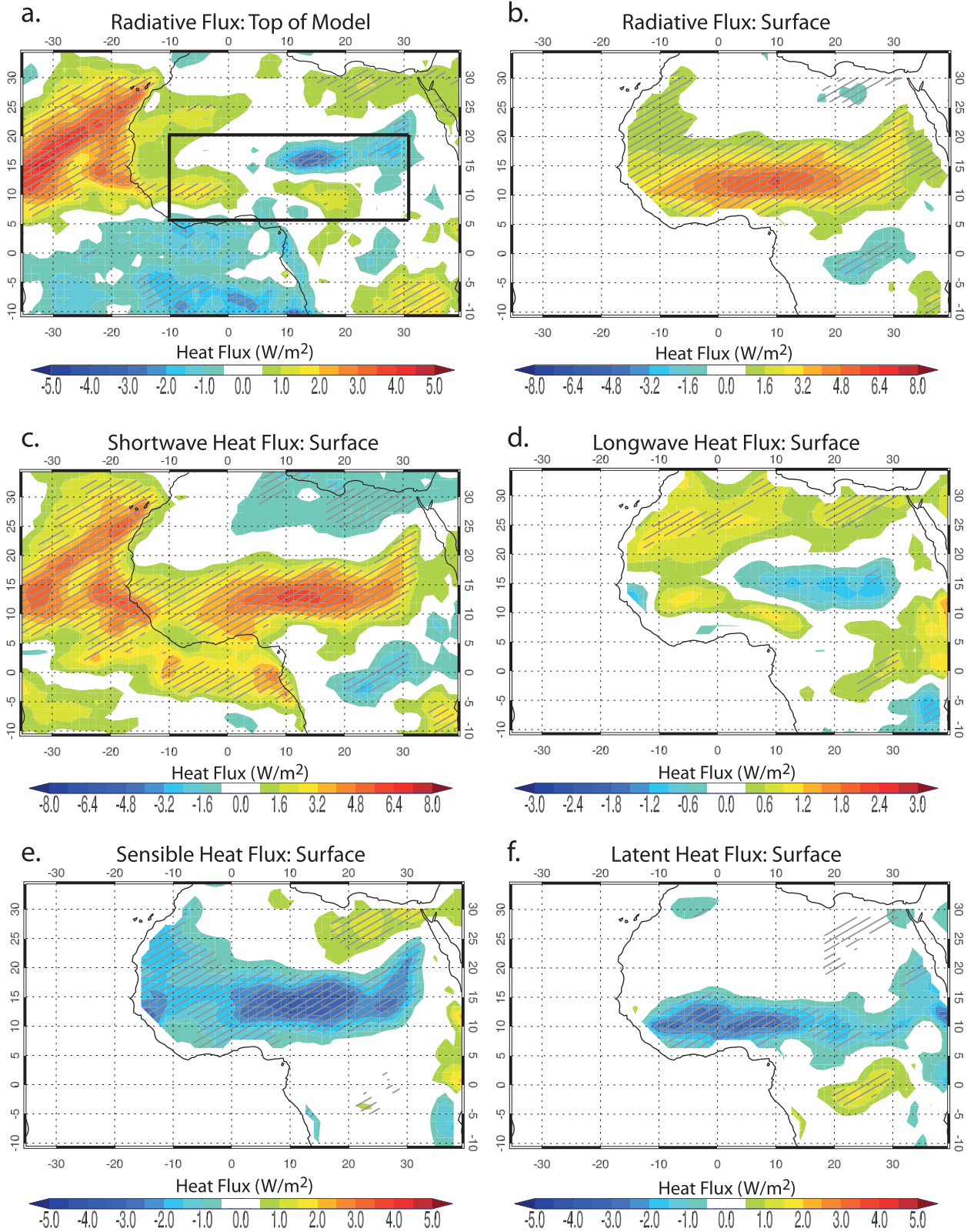
Figure 8a shows the regression of land surface temperature over North Africa on the dust index. The upward flux of shortwave radiation significantly cools the land surface in tropical Africa (Fig. 8a). This result is consistent with other studies (e.g., Yoshioka et al. 2007; Prospero and Lamb 2003; Mahowald et al. 2010), where an increase in dust aerosols causes a cooling of the North African region. Since the SSTs are prescribed in our experimental setup, a cooling of the West African landmass

reduces the land–sea temperature gradient. This results in a weakening of the African monsoons, as indicated by reduction of precipitation over equatorial West Africa and an increase in rainfall over the Gulf of Guinea (Fig. 8b). Dust aerosols over the Sahel also tend to increase the diabatic heating of the lower troposphere (Fig. 8c), which further helps to reduce convection in the region and prevents the northward movement of the ITCZ, increasing precipitation southward over the equatorial Atlantic ocean. The reduction of African monsoon caused by increase in dust aerosols is also observed in other modeling studies (Mahowald et al. 2010; Yoshioka et al. 2007). A corresponding significant increase in cloud cover is also noted over the Gulf of Guinea (Fig. 8d). While there is a significant increase in high clouds associated with deep convection over the equatorial Atlantic (Fig. 8e), there is an increase in the low clouds over the northern tropical Atlantic (Fig. 8f). Warming of the free troposphere by dust aerosols reduces the lower tropospheric instability, which results in the increase in stratocumulus clouds. These shallow clouds increase the reflection of shortwave radiation back to space as is seen in Fig. 7a. Abundant carbonaceous aerosols over the southeastern tropical Atlantic also have a similar impact of the marine stratocumulus clouds there, as discussed in more detail in the following sections.

#### *b. Carbonaceous aerosol–induced climate variability*

The largest variability of carbonaceous aerosol resulting from variability in wildfire emissions over central Africa is observed over southwest equatorial Africa in the dry boreal summer months in CAM4 as indicated by the box in Fig. 9a. Figure 9a shows a regression of radiative heat flux at the TOM over Africa on an index of black carbon aerosol optical depth for the period 1961–2000 for the AMIP-CMIP5AERO + RETRO ensemble. The black carbon aerosol index is defined as the regionally averaged black carbon optical depth averaged over southwest equatorial Africa ( $15^{\circ}$ – $0^{\circ}$ S,  $10^{\circ}$ – $25^{\circ}$ E) in the boreal summer season. An increase in black carbon over the south equatorial African region is associated with an increase of net outgoing radiative flux over the southeastern tropical and equatorial Atlantic Ocean, primarily because of the reflection by increased low cloud cover as discussed later in the section.

There is a large net upward surface net radiative heat flux over land as seen in Fig. 9b. The difference between Figs. 9a and 9b (not shown) represents the amount of heat flux into the atmosphere that has been absorbed by the carbonaceous aerosols. Figures 9c and 9d show the regression of the components of the net surface radiative heat flux. An increase of the upward flux of surface shortwave radiation is caused by the absorption of



shortwave radiation by tropospheric black carbon. The decrease in surface longwave radiation is primarily associated with a reduction in surface temperature. An associated decrease in the loss of heat by sensible heat flux and latent heat flux is also noted over the south tropical African region (Figs. 9e,f).

Figure 10a shows a regression of summer land surface temperature over Africa on the black carbon index for the period 1961–2000. Statistically significant cooling over the southeastern equatorial African region is primarily caused by the reduced incoming shortwave radiation at the surface (Fig. 9c). Tropospheric black carbon also results in an increase in the atmospheric shortwave heating over the equatorial and south tropical Atlantic Ocean and Africa in the experiment (Fig. 10b). The tropospheric heating over land is closer to the surface, where the aerosols reside, whereas over the oceans the diabatic heating occurs above the marine stratocumulus cloud deck in the model (not shown), similar to observed data over the region (e.g., Wilcox 2010). Convective precipitation over the tropical Atlantic and West Africa monsoon is not coherent (not shown), and there is a reduction over the African landmass east of the Gulf of Guinea associated with an increase in black carbon aerosols, similar to other coupled model studies (e.g., Huang et al. 2009a).

An increase in the total cloud fraction is mainly caused by the increase in low cloud cover in the marine stratocumulus region in the southeast equatorial Atlantic (Figs. 10c,d) in our experiment. The increase in marine stratocumulus is primarily caused by the intensification of the inversion layer above the boundary layer due to heating of the free troposphere by absorbing carbonaceous aerosols that lie above the marine cloud deck in the region (e.g., Johnson et al. 2004). An increase in carbonaceous aerosols is also associated with a decrease in significant middle troposphere subsidence over the southeast tropical Atlantic in AMIP-CMIP5AERO + RETRO (not shown). Reduction in subsidence in the southeast tropical Atlantic is associated with a deepening of the boundary layer, which results in a reduction of low cloud cover in both observations (Wood and Hartmann 2006) and models (Sakaeda et al. 2011). However, the increase in low cloud cover in our

experiment suggests that the effect of subsidence is weak in the model. We will discuss more on marine stratocumulus as they are strongly coupled to the ocean surface state in the next section.

Thermodynamic coupling between the atmosphere and the ocean is known to dominate climate variability of tropical Atlantic and its surrounding regions. The absence of thermodynamic feedbacks between the atmosphere and the ocean in the experiments discussed above constrains the ocean from responding to aerosol-induced radiative forcings, so the prescribed SSTs can unduly control the climate of the region. The response of the tropical Atlantic and West Africa to aerosol forcings has been found to be amplified in simulations of atmosphere models coupled to a slab ocean model (e.g., Yoshioka et al. 2007). In the next section, we investigate the response to aerosol forcings in the presence of active thermodynamic coupling between the atmosphere and ocean.

## 8. Role of atmosphere–ocean thermodynamic feedbacks

### a. Experimental setup

We perform two experiments with CAM4 coupled to a slab ocean model (CAM4-SOM) to isolate the role of the ocean mixed layer in the interaction of aerosols with the climate system. The SOM contains an ocean prescribed with a finite mixed layer depth varying geographically. The SOM lacks ocean dynamics and interacts with the atmosphere only thermodynamically by exchanging heat fluxes. The lack of ocean dynamics in the model is compensated by prescribing a climatology of implied heat flux ( $Q$ ) that represents deep water exchange and horizontal transport. For our CAM4-SOM simulations, the  $Q$  fluxes are computed from a fully coupled atmosphere–ocean model preindustrial control simulation climatology. More details on the SOM component of CESM1.0 can be found in Neale et al. (2010). Atmosphere models coupled to SOMs have been shown to capture physical thermodynamic processes over the tropical Atlantic fairly well (e.g., Saravanan and Chang 2004; Mahajan et al. 2009, 2010).

←

FIG. 7. Dust aerosol-induced heat flux variability over the north tropical Atlantic and North Africa in the AMIP-CMIP5AERO + RETRO experiment. Regression of spring season (a) net radiative flux at the top of the model, (b) net radiative heat flux at the surface, (c) shortwave heat flux at the surface, (d) longwave heat flux over land surface, (e) sensible heat flux over land surface, and (f) latent heat flux over land surface (all in units of  $\text{W m}^{-2}$ ) on the standardized time series (zero mean and unit standard deviation) of spring season dust optical depth averaged over a region in tropical North Africa [indicated by the rectangular box in (a)] for the period 1961–2000. Upward heat fluxes are defined to be positive. Hatched areas represent regions where the regression coefficients are statistically significant at the 95% confidence level based on a two-tailed  $t$  test.

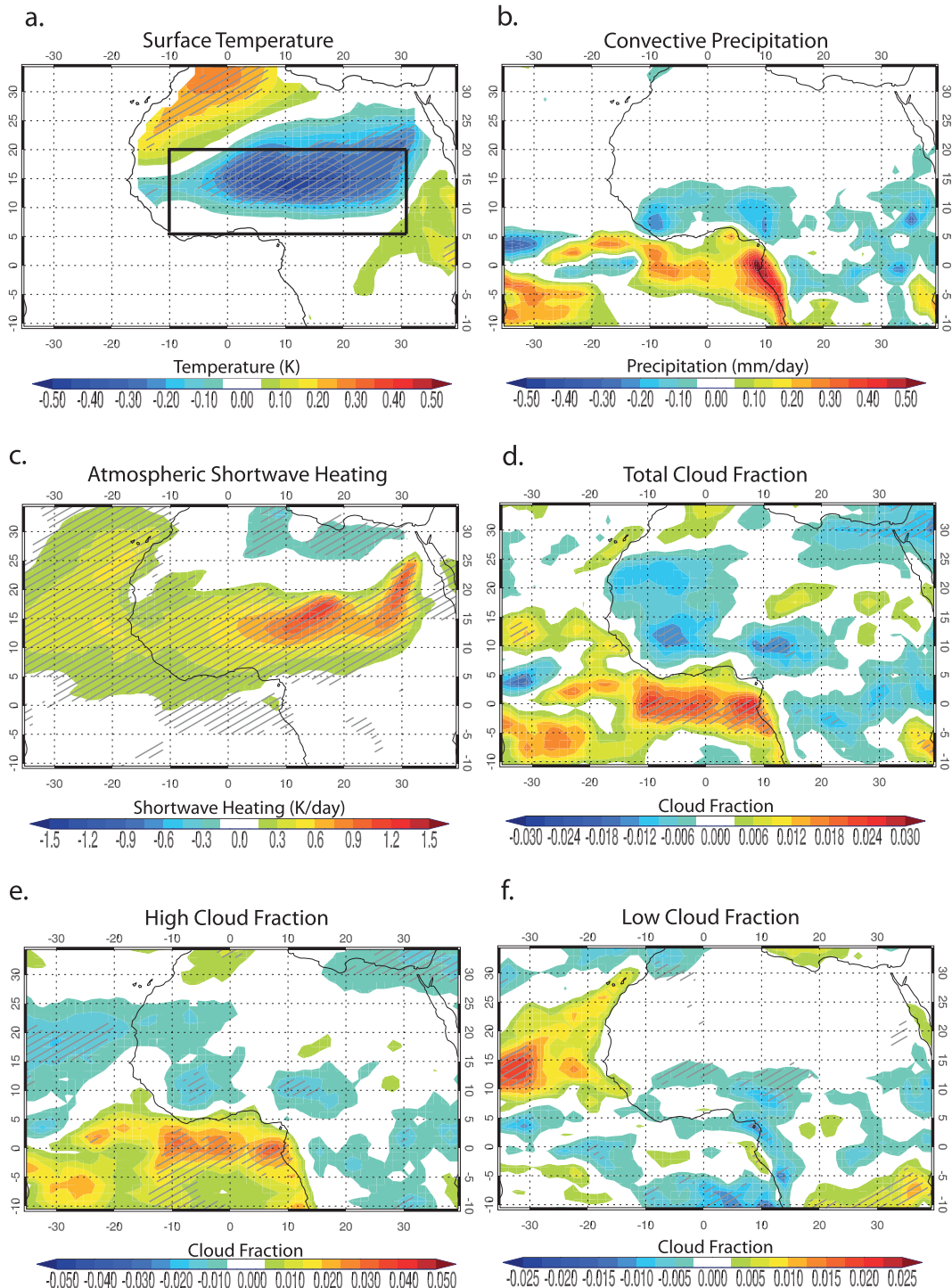


FIG. 8. Dust-associated variability over northern tropical Atlantic and North Africa in the AMIP-CMIP5AERO + RETRO experiment. As in Fig. 7, but for (a) surface temperature (K), (b) convective precipitation ( $\text{mm day}^{-1}$ ), (c) vertically integrated atmospheric shortwave diabatic heating rate ( $\text{K day}^{-1}$ ), (d) total cloud fraction (vertically integrated above 400-mb pressure level), and (e) high cloud fraction (vertically integrated between surface and 700-mb pressure levels). Hatched areas in (a) and (c)–(f) represent regions where the regression coefficients are statistically significant at the 95% confidence level based on a two-tailed  $t$  test.

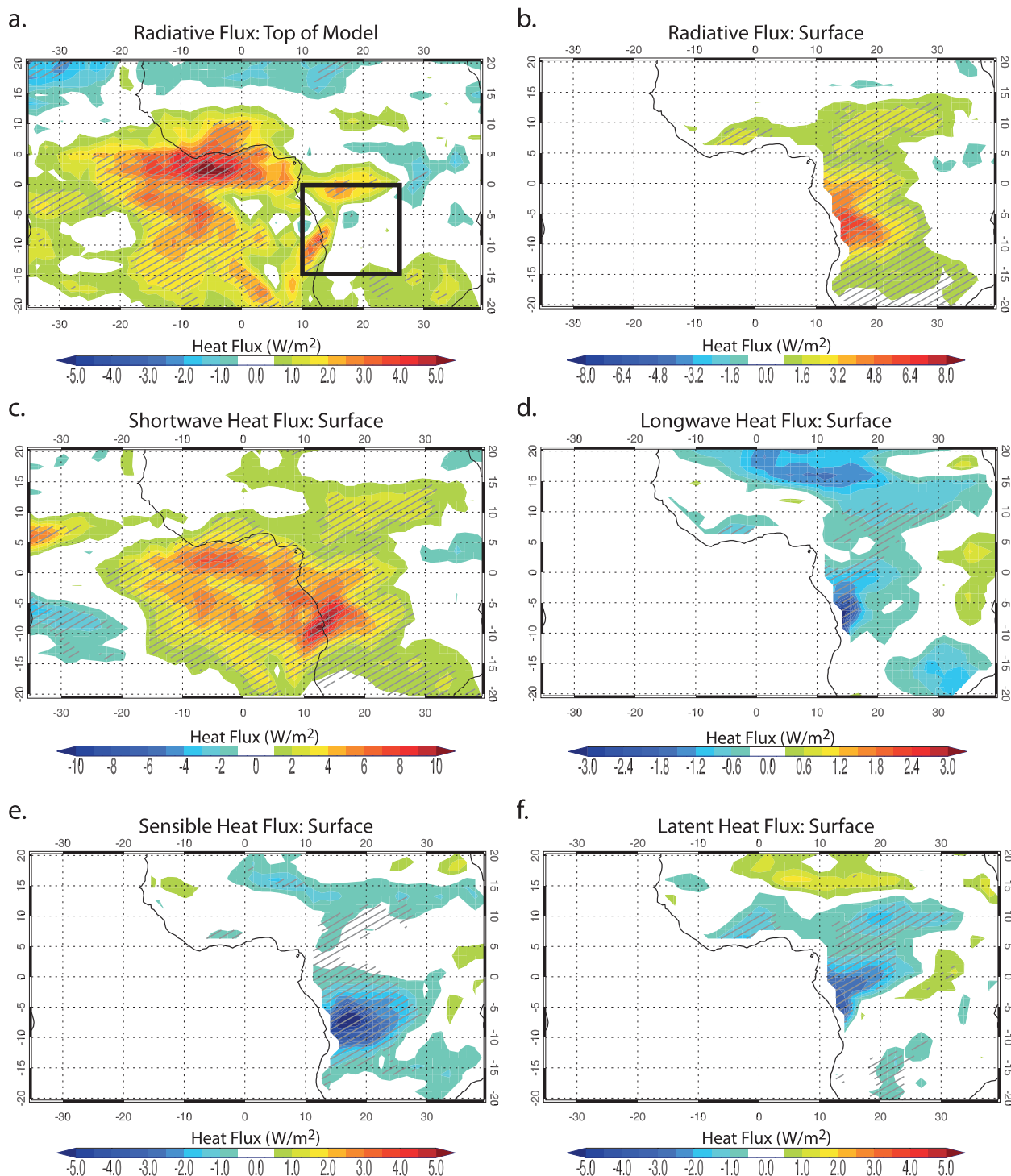


FIG. 9. Black carbon-induced heat fluxes over tropical Atlantic and West Africa in the AMIP-CMIP5AERO + RETRO experiment. Regression of summer season (a) net radiative flux at the top of the model, (b) net radiative heat flux at the surface, (c) shortwave heat flux at the surface, (d) longwave heat flux over land surface, (e) sensible heat flux over land surface, and (f) latent heat flux over land surface (all in  $\text{W m}^{-2}$ ) on the standardized time series (zero mean and unit standard deviation) of summer black carbon optical depth averaged over the southwest equatorial Africa [indicated by the rectangular box in (a)] for the period 1961–2000. Upward heat fluxes are defined to be positive. Hatched areas represent regions where the regression coefficients are statistically significant at the 95% confidence level based on a two-tailed  $t$  test.

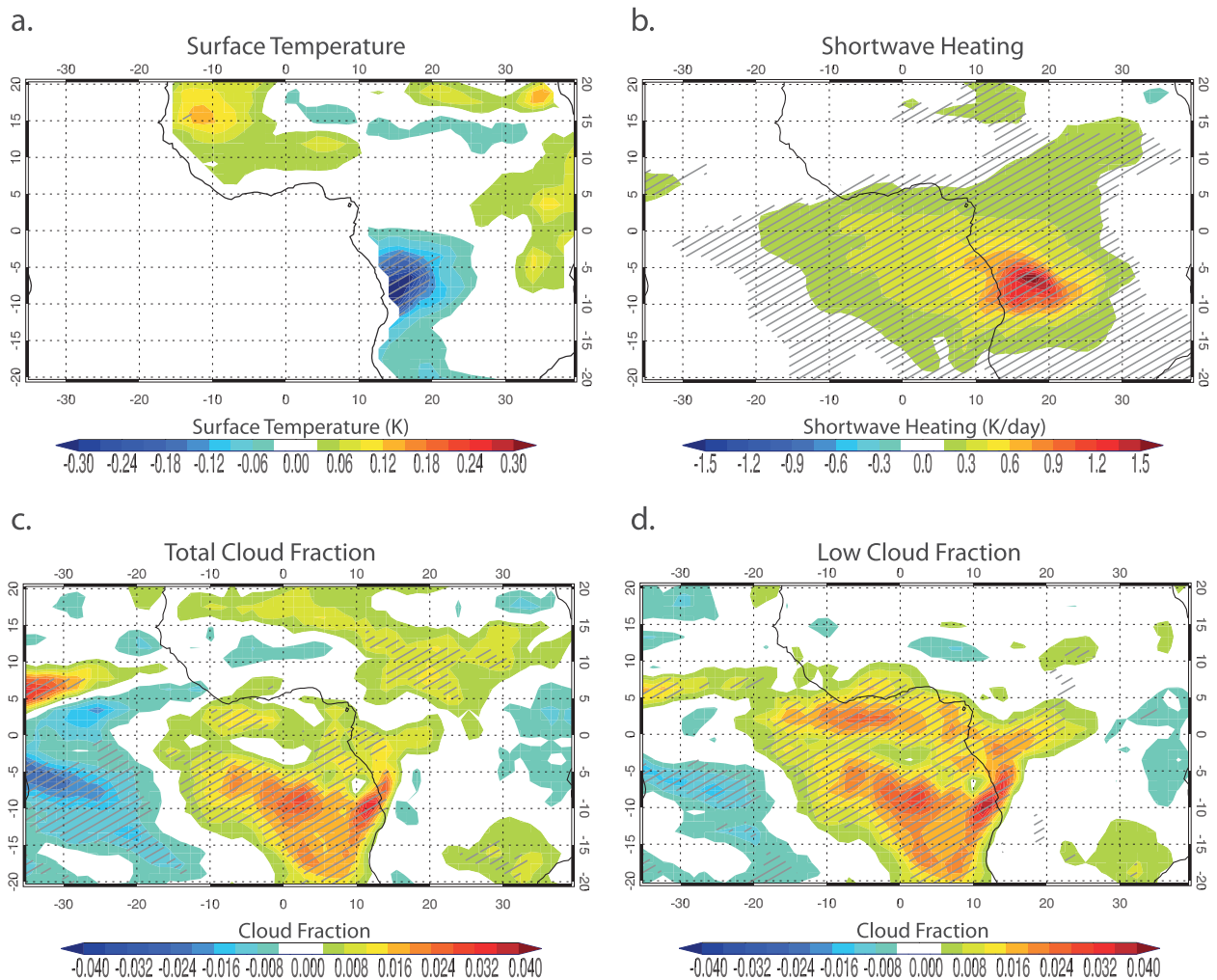


FIG. 10. Black carbon associated variability over tropical Atlantic and West Africa in the AMIP-CMIP5AERO + RETRO experiment. As in Fig. 9, but for (a) surface temperature (K), (b) vertically integrated atmospheric shortwave diabatic heating rate ( $\text{K day}^{-1}$ ), (c) total cloud fraction, and (d) low cloud fraction (vertically integrated between surface and 700-mb pressure levels).

In the first CAM4-SOM experiment, we prescribe the model with a climatology of present-day aerosol loadings. The tropospheric aerosol climatology is created from the new CMIP5-RETRO aerosol dataset (section 3) for the period 1981–2000. This experiment is termed the CAM4-SOM-20AERO experiment. In the second experiment, the same model is forced with a climatology of the preindustrial aerosol distribution, as in the experiment AMIP-1850AERO. We refer to this experiment as CAM4-SOM-1850AERO. Both simulations are run for 40 years and the analysis is performed on the last 30 years of the runs, discarding the first 10 years as model spinup time.

Figure 11 shows the spatial pattern of the difference in the total aerosol optical depth and the optical depth of the individual species in the boreal summer season between the present day and the preindustrial era runs

averaged over the 30-yr experimental period. Figure 11 shows the presence of more sulfate aerosols covering all of the Northern Hemisphere (Fig. 11b) and large amounts of absorbing carbonaceous aerosols lying over eastern equatorial Pacific and Atlantic Oceans originating in South America and south equatorial Africa in the present-day run (Figs. 11c,d). Increased carbonaceous aerosols are also seen over the Southeast Asian region and East Asia in the present-day era with respect to the preindustrial era (Figs. 11c,d). A substantial decline of organic carbon is noted over the eastern coast of North America in the summer season of the present-day era as compared to the preindustrial era (Fig. 11d). Dust aerosol and sea salt aerosol optical depths show some difference between the two eras in the summer season (Figs. 11e,f), with larger differences in the other seasons.

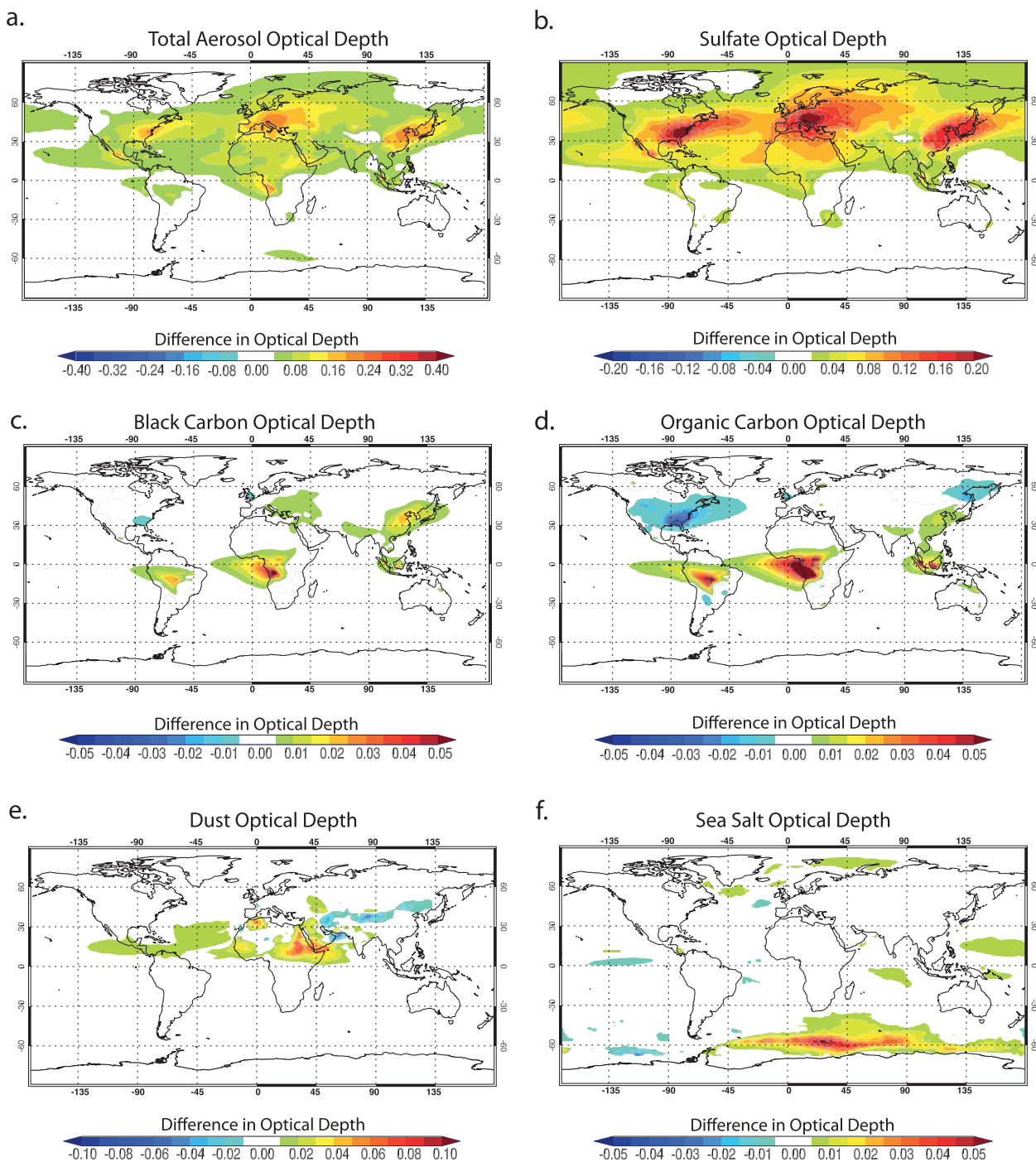


FIG. 11. Difference (CAM4-SOM-20AERO – CAM4-SOM-1850AERO) in aerosol optical depth for simulations of CAM4 coupled to a slab ocean model prescribed with 1981–2000 climatology (CAM4-SOM-20AERO) and preindustrial climatology of aerosols (CAM4-SOM-1850AERO) for (a) all, (b) sulfate (c) black carbon, (d) organic carbon, (e) dust, and (f) sea salt aerosols.

Figure 12 shows the vertical profile of the zonally averaged difference in the sulfate, black carbon, organic carbon, and dust aerosol loadings between the two aerosol climatologies prescribed in the CAM4-SOM

experiments for the boreal summer season (averaged over June–August) over the tropical Atlantic Ocean (35°S–35°N, 60°W–15°E; ocean-only grid points). The largest differences in aerosols over the tropical Atlantic

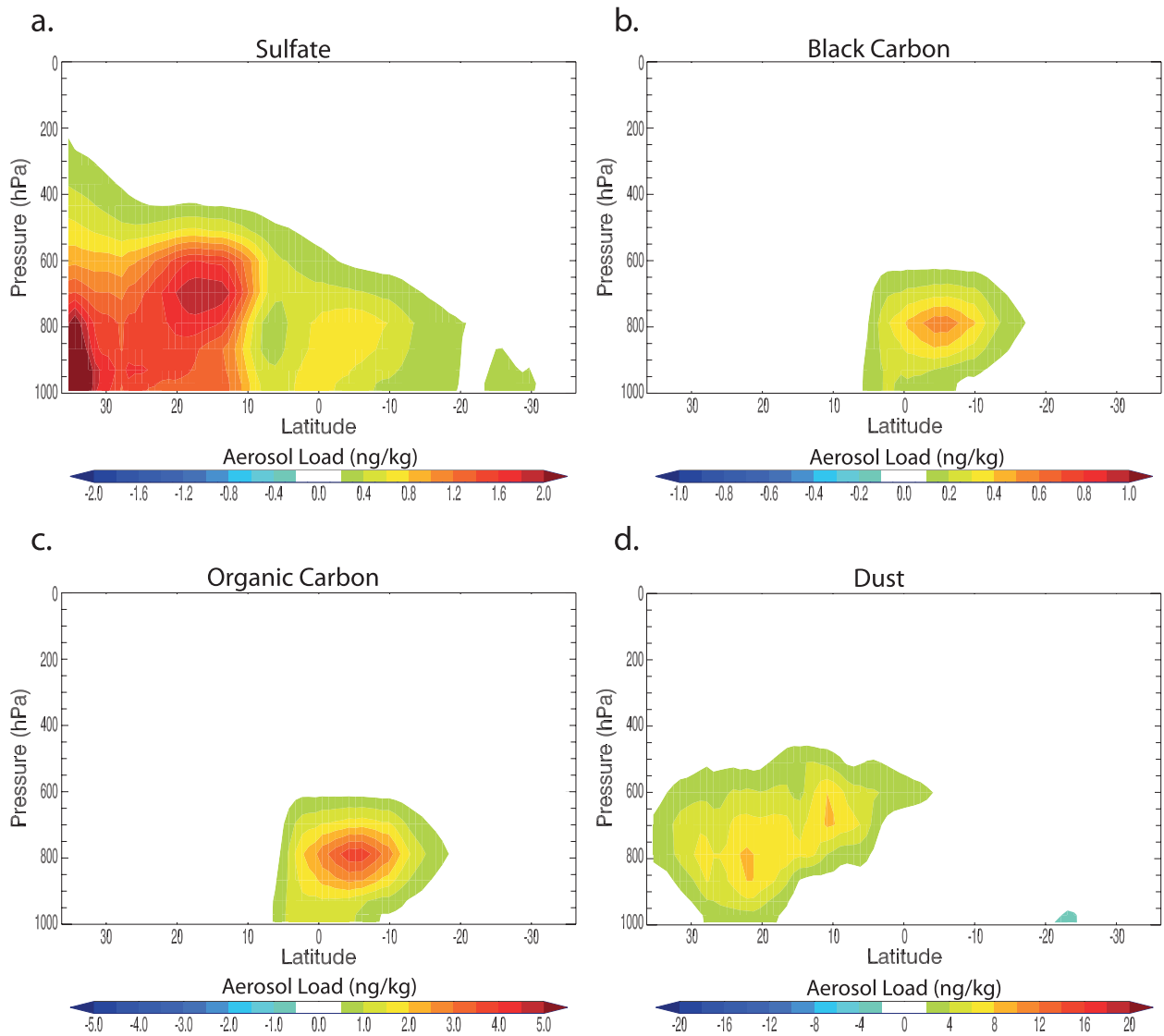


FIG. 12. Vertical profile of the difference (CAM4-SOM-20AERO – CAM4-SOM-1850AERO) in aerosol loadings zonally averaged over the tropical Atlantic Ocean in the boreal summer season for simulations of CAM4 coupled to a slab ocean model prescribed with 1981–2000 climatology (CAM4-SOM-20AERO) and preindustrial climatology of aerosols (CAM4-SOM-1850AERO) for (a) sulfate, (b) black carbon, (c) organic carbon, and (d) dust aerosols.

occur in the boreal summer season between the present-day and the preindustrial era, particularly for sulfate and carbonaceous aerosols in the free troposphere. In the present-day dataset, the sulfate aerosol loadings are larger over the northern tropical Atlantic (Fig. 12a), whereas the carbonaceous aerosol loadings are larger above the boundary layer over the southern equatorial Atlantic (Figs. 12b,c) because of the increased biomass burning in southwest equatorial Africa in the present-day era. The vertical profile of dust (Fig. 12d) and sea salt loadings (as suggested in Fig. 11f) are largely similar in the two eras in the summer season with little more

dust over the north tropical Atlantic, and larger differences in the other seasons.

### b. ITCZ

In response to the surface radiative forcing induced by the greater amount of aerosols in the present day era, the land surface temperature in the SOM experiment responds by cooling significantly (Fig. 13a). This response is similar to the cooling associated with increasing dust or carbonaceous aerosols in the AMIP experiments. In addition, the mixed layer of the SOM actively responds to the surface radiative forcings. However, the magnitude of

the response over the ocean is much smaller, owing to the larger specific heat of water in the CAM4-SOM-20AERO run.

Climatologically, the ITCZ, which is very sensitive and nonlinearly related to the underlying SSTs over the Atlantic Ocean, hovers between 5° and 10°N in the boreal summer season owing to the development of the cold tongue in the southeastern equatorial Atlantic and the onset of the African monsoon (e.g., Xie and Carton 2004). With the cooling of the north tropical Atlantic, the rainfall in the eastern ITCZ band shows a reduction in the CAM4-SOM-20AERO simulation as compared to the CAM4-SOM-1850AERO simulation, with an increase in rainfall over the southern equatorial Atlantic Ocean (Fig. 13b). The southward shift in the ITCZ in CAM4-SOM-20AERO is associated with an increase in cloud cover in the southern equatorial Atlantic as compared to the CAM4-SOM-1850AERO run (Fig. 13c). Further, the stronger cooling of the North African landmass also reduces the land–sea temperature contrast, which prevents the rainband from moving toward the land, diminishes convection over West Africa and the north tropical Atlantic, and increases deep convection over south tropical Atlantic (Fig. 13b).

The presence of increased tropospheric carbonaceous aerosols over the southern tropical Atlantic in the CAM4-SOM-20AERO simulation causes heating of the troposphere over the south equatorial Atlantic and southwest equatorial Africa (Fig. 13d). Figure 14a shows the mean vertical profile of zonally averaged total cloud fraction over the tropical Atlantic (35°S–35°N, 60°W–15°E; ocean-only grid points) in CAM4-SOM-1850AERO. Figures 14b and 14c show the difference in the convective clouds and atmospheric shortwave heating between CAM4-SOM-20AERO and CAM4-SOM-1850AERO simulations. A southward cross-equatorial shift in tropical deep convection is associated with a shift of the ITCZ (Fig. 14c), with a statistically significant increase in southern equatorial deep convective clouds. The decrease in convective clouds over the northern equatorial Atlantic is, however, not significant at the 95% confidence level. A strong, statistically significant diabatic heating occurs over the equatorial and south tropical Atlantic Ocean with the heating mostly constrained between the surface and 600-mb pressure level (Fig. 14d). The diabatic heating of the southern equatorial Atlantic lower troposphere zonally occurs over regions of increased convection, suggesting that the increase in static stability (e.g., Ramanathan et al. 2005) cannot prevent the induced shifting of the ITCZ by cooling of the Northern Hemisphere, but could only perhaps reduce it. However, the weak diabatic heating over the north equatorial Atlantic supports the weakening of convection there.

### c. Marine stratocumulus

The marine stratocumulus clouds are also closely tied to the underlying SSTs, with lower SSTs resulting in more stratocumulus clouds. In response to the increase in carbonaceous aerosols over the southeast tropical Atlantic ocean, there is a reduction in the SSTs in the region by about 0.2 K (as indicated by the surface air temperature in Fig. 13a) in the CAM4-SOM-20AERO simulation, although not statistically significant at the 95% confidence level. The cooler SSTs tend to induce further generation of stratocumulus clouds owing to the SST–stratocumulus cloud feedback (Philander et al. 1996). Figure 13c shows the increase in the total cloud fraction over the southeastern tropical Atlantic. A partitioning of the total cloud fraction reveals that the increase in the total cloud fraction over the southeastern tropical Atlantic is essentially caused by the increase in the low-level nonconvective clouds (not shown) as in the AMIP-CMIP5AERO + RETRO experiment set. The increase in the low-level stratocumulus clouds then results in reducing the underlying SSTs further. In the absence of SST–stratocumulus cloud feedback, as in the AMIP-CMIP5AERO + RETRO run, an increase in the aerosols would result in a weaker response of the marine stratocumulus.

The marine stratocumulus cloud fraction in CAM4 is parameterized to be dependent on the lower tropospheric stability (LTS). The LTS is defined as the difference in potential temperature at the 700-mb atmospheric level and the surface potential temperature in a vertical column. The marine stratocumulus cloud fraction increases by 0.057 for each degree rise in  $(\theta_{700} - \theta_s)$ , and forms in the model atmospheric layer below the strongest stability jump between model layers between 750 mb and the surface (Neale et al. 2010). The peak anomalous diabatic heating occurs at the 800-mb pressure level in CAM4-SOM-20AERO over the southeastern tropical Atlantic ocean, which is above the marine stratus cloud deck there (Fig. 14a). This anomalous diabatic heating above the 800-mb layer in the region (Fig. 14c) results in an increase in the marine stratocumulus in the model. A cooling of the ocean mixed layer because of reduced shortwave heating at the surface resulting from the increase in low-level cloud cover further amplifies the difference  $\theta_{700} - \theta_s$ , which then further increases the marine stratocumulus cloud fraction.

The increase in marine stratocumulus in the presence of black carbon aerosols has been observed over the region (e.g., Kaufman et al. 2005), suggesting that the parameterization of marine stratocumulus clouds is able to capture this physical phenomenon in CAM4 realistically. Sakaeda et al. (2011) find that the sign of low cloud cover is a robust response of CAM3-SOM. They

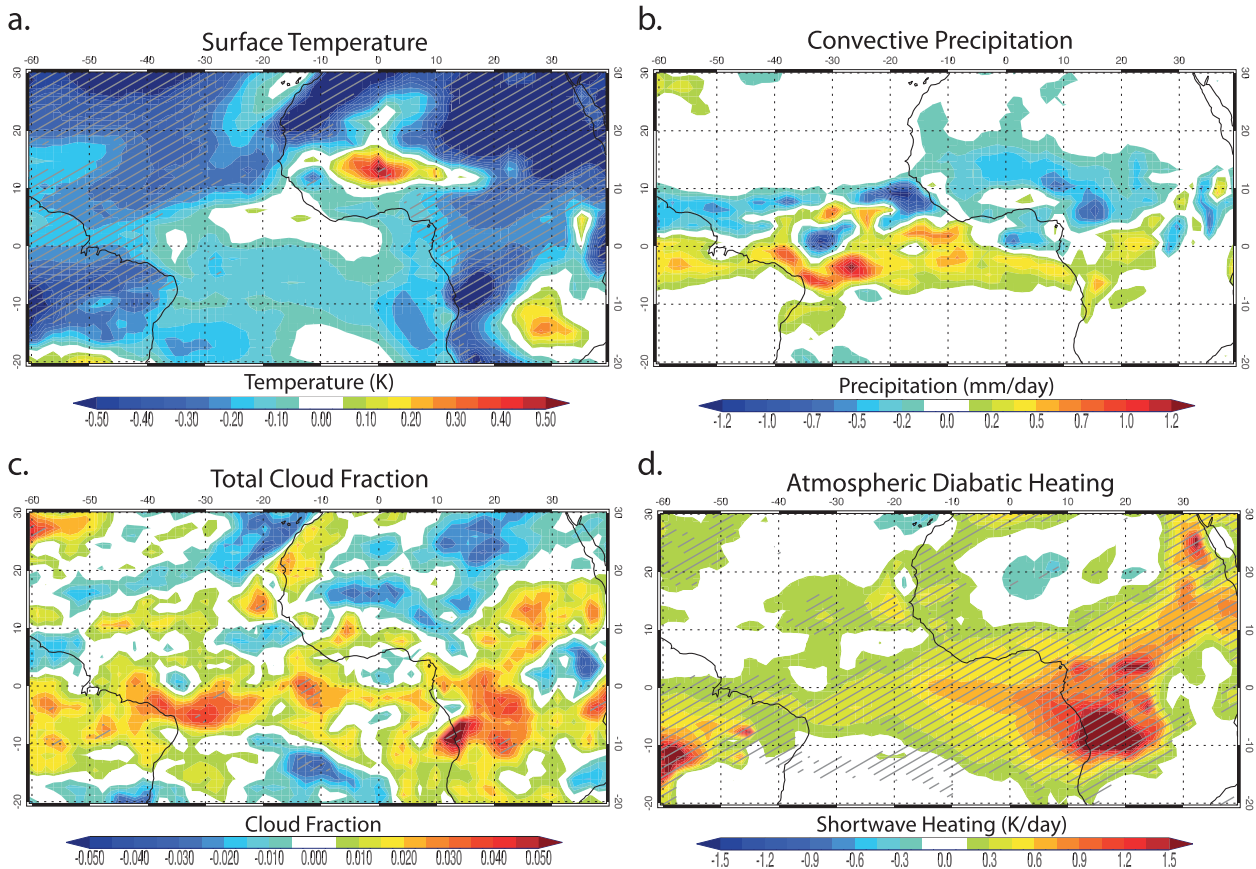


FIG. 13. Response of the CAM4-SOM model to aerosol radiative forcing. Difference (CAM4-SOM-20AERO – CAM4-SOM-1850AERO) in the mean (a) surface temperature, (b) convective precipitation ( $\text{mm day}^{-1}$ ), (c) total cloud fraction, and (d) vertically integrated atmospheric shortwave heating rate ( $\text{K day}^{-1}$ ) in the boreal summer season averaged over 30 yr between the CAM4-SOM-20AERO and CAM4-SOM-1850AERO simulations. Hatched areas in (a), (c), and (d) represent regions where the differences are statistically significant at the 95% confidence level based on a two-tailed  $t$  test.

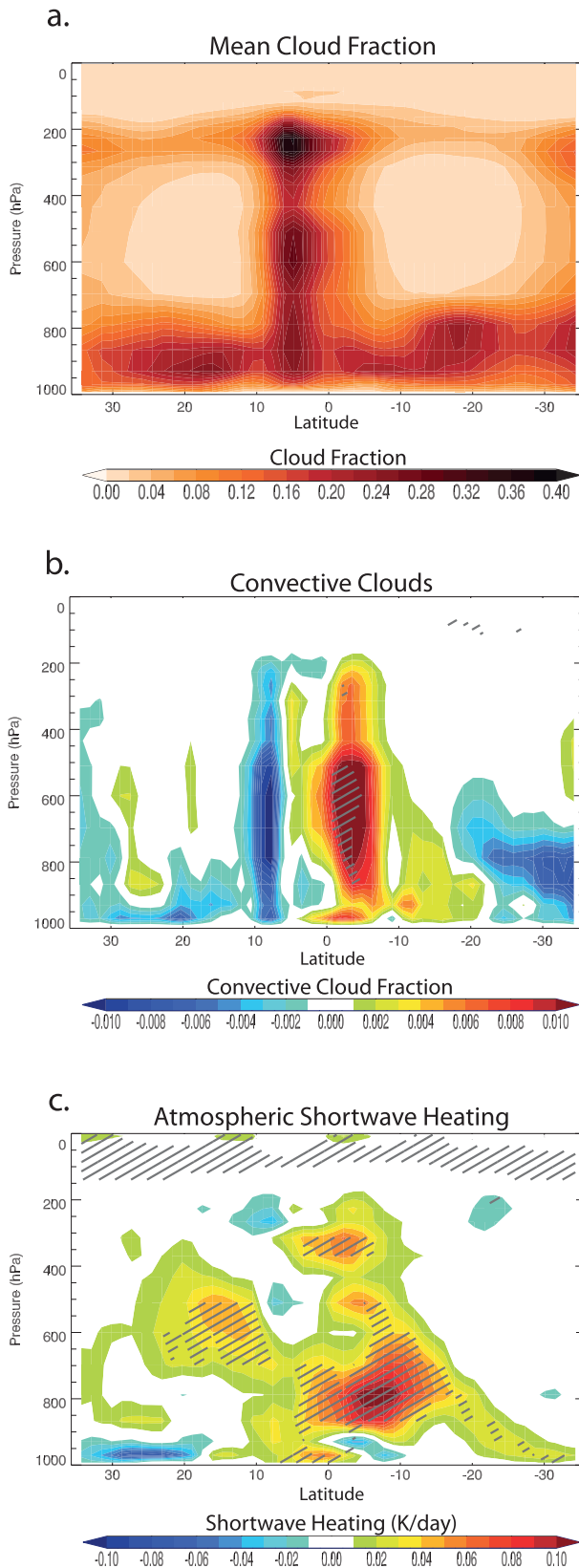
found that only the magnitude of the low cloud cover is sensitive to the choice of parameterization of the low cloud cover. However, the presence of atmosphere–ocean thermodynamic feedbacks is important for a credible simulation of marine stratocumulus. In a prescribed SST experiment forced with present-day aerosols and the SST climatology used to compute the  $Q$  fluxes for the CAM4-SOM experiments, the marine stratocumulus low cloud fraction is found to be significantly lower than in CAM4-SOM-20AERO at the 95% confidence level (not shown).

## 9. Summary and discussion

We have generated a new high-resolution ( $0.9^\circ \times 1.25^\circ$ ) tropospheric aerosol dataset for the period 1961–2000 with monthly temporal resolution using CMIP5 surface emissions data combined with RETRO wildfire surface emissions data. The use of RETRO wildfire data

introduces interannual variability component to the decadal-resolution CMIP5 surface emissions data. It should be noted, however, that wildfire data bear large uncertainties (Schultz et al. 2008). Nonetheless, this study is the first attempt to generate a realistic monthly resolved aerosol radiative forcing in twentieth-century climate models simulations that are otherwise prescribed with decadal tropospheric aerosol distributions.

Twentieth-century prescribed SST and sea ice experiments using the new aerosol dataset reveal that direct and semidirect effects of aerosols alone can induce significant interannual variability in regional climate. Regression analysis over tropical Atlantic and Africa indicates that dust and carbonaceous aerosols can modulate surface temperature, precipitation, and cloud cover over the region. Aerosol optical depth over the tropical Atlantic and the African continent has been found to be weakly correlated with climate phenomena such as the North Atlantic oscillation, Pacific decadal



oscillation, El Niño, Atlantic meridional mode, and Atlantic Niño. These climate modes are also known to modulate the climate of the tropical Atlantic and the African continent (e.g., Xie and Carton 2004, and references therein). Hence, our regression analysis in section 7 could have resulted in spurious elevated coefficients. However, results from multivariate regression analysis following Huang et al. (2009a), which removes coherent signals between aerosol optical depth and other variables caused by these climate phenomena, are similar to what we find in section 7, suggesting little forced coherence between aerosols and the climate of tropical Atlantic and Africa in CAM4.

We find that dust variability can significantly affect rainfall over the West African landmass by surface cooling and diabatic heating of the troposphere, supporting the result that years with large dust emissions tend to be associated with less rainfall in the West African region (Mahowald et al. 2010). However, dust emissions and dust aerosol optical depth are difficult to capture from satellite retrievals and models (Mahowald et al. 2006b). An improvement in dust estimation and predictions could hence also improve climate prediction over the region. As a caveat, recent in situ measurements of dust over the Sahara and Asia suggest that the single scattering albedo of dust lies in the range of 0.90 to 0.99. The result suggests that it is unlikely that the dust could be strongly absorbing in the shortwave and visible range, implying that the direct radiative forcing associated with dust is essentially negative, much like other scattering aerosols (e.g., Forster et al. 2007). However, it is strongly absorbing in the longwave radiation range, which would induce a positive radiative forcing. In CAM4, the optical properties of dust allow for absorption in the shortwave but not in the longwave radiation range. The impacts of correcting for the optical properties of dust on our simulation results are hard to predict and future experiments would be required to accurately identify dust radiative impacts.

We also find that the presence of carbonaceous aerosols can significantly increase the marine stratocumulus

←

FIG. 14. (a) Vertical profile of zonally averaged clouds in CAM4-SOM-1850AERO over the tropical Atlantic Ocean (35°N–35°S, 60°W–15°E; ocean-only grid points) in boreal summer, and vertical profile of the difference (CAM4-SOM-20AERO – CAM4-SOM-1850AERO) of zonally averaged (b) convective clouds and (c) atmospheric heating rate ( $\text{K day}^{-1}$ ) over the tropical Atlantic in boreal summer between the CAM4-SOM-20AERO and CAM4-SOM-1850AERO simulations. Hatched areas in (b) and (c) represent regions where the differences are statistically significant at the 95% confidence level based on a two-tailed  $t$  test.

cloud cover over the southeastern tropical Atlantic Ocean and this effect is amplified in the presence of air–sea thermodynamic feedbacks. This result is consistent with those of other studies (e.g., Kaufman et al. 2005; Huang et al. 2009a; Sakaeda et al. 2011). Based on an analysis of satellite data, Kaufman et al. (2005) suggest that in regions dominated by shallow clouds, such as the southern and northern tropical Atlantic, the presence of aerosols also results in reduced droplet size in shallow clouds, resulting in inhibited precipitation and an enhanced cloud cover. CAM4 physics only simulates the direct and semidirect effect of aerosols and hence the enhancement of clouds that we see over the south tropical Atlantic is solely due to those effects. Our estimate of the influence of aerosols over the south tropical Atlantic marine stratocumulus clouds, although significant, is thus still a conservative estimate. However, vertical profile measurements over the region during the Southern African Regional Science Initiative Campaign (SAFARI) 2000 experiment in September 2002 (Haywood et al. 2003) and satellite lidar measurements (Wilcox 2010; Chand et al. 2009) reveal that aerosols over the ocean in the southeastern tropical Atlantic region are clearly separated from the underlying stratocumulus clouds by the inversion layer, restricting aerosol–cloud microphysical interactions and suggesting limited local aerosol indirect effect over the ocean in the region.

In the presence of sulfate aerosols over the northern tropical Atlantic and North Africa, CAM4-SOM simulates a southward shift of the ITCZ even in the presence of carbonaceous aerosols over the southern tropical Atlantic. A recent study by Huang et al. (2009a) suggests that the relationship between carbonaceous aerosols and precipitation over the equatorial Atlantic and West Africa may not be linear. Our tropospheric aerosol dataset underestimates the amount of carbonaceous aerosols over the south tropical Atlantic/Africa as compared to MODIS estimates (Fig. 1). A larger amount of carbonaceous aerosols over the region could result in a larger diabatic heating over the southern equatorial Atlantic Ocean, opposing the southward shift of the ITCZ, perhaps nonlinearly. But, given the strong coupling between ITCZ and SST, it appears unlikely that the diabatic heating would be able to overwhelm the effects of SST on the ITCZ and prevent the migration of the ITCZ.

Carbonaceous aerosols have been found to play a significant role in the climate of other regions of the world, particularly Southeast Asia and South America and the adjacent eastern Pacific Ocean. We plan to isolate the aerosol-induced interannual regional climate variability in these regions using the new high-resolution monthly CMIP5-RETRO aerosol tropospheric distribution dataset that we have generated in this study in the near future.

**Acknowledgments.** This work was funded by a grant from the Office of Science [Biological and Environmental Research (BER)] of the U.S. Department of Energy (DOE). This work was partially supported by the DOE under the SciDAC program. Oak Ridge National Laboratory is managed by UT-Battelle, LLC, for the U.S. Department of Energy under Contract DE-AC05-00OR22725. This research used resources of the Oak Ridge Leadership Computing Facility at the Oak Ridge National Laboratory, which is supported by the Office of Science of the U.S. Department of Energy under Contract DE-AC05-00OR22725. The CESM project is supported by the National Science Foundation and the Office of Science (BER) of the U.S. Department of Energy.

## REFERENCES

- Ackerman, A. S., O. B. Toon, D. E. Stevens, A. J. Heymsfield, V. Ramanathan, and E. J. Welton, 2000: Reduction of tropical cloudiness by soot. *Science*, **288**, 1042–1047, doi:10.1126/science.288.5468.1042.
- Albrecht, B. A., 1989: Aerosols, cloud microphysics, and fractional cloudiness. *Science*, **245**, 1227–1230, doi:10.1126/science.245.4923.1227.
- Bond, T. C., D. G. Streets, K. F. Yarber, S. M. Nelson, J.-H. Woo, and Z. Klimont, 2004: A technology-based global inventory of black and organic carbon emissions from combustion. *J. Geophys. Res.*, **109**, D14203, doi:10.1029/2003JD003697.
- Chand, D., R. Wood, T. L. Anderson, S. K. Satheesh, and R. J. Charlson, 2009: Satellite-derived direct radiative effect of aerosols dependent on cloud cover. *Nat. Geosci.*, **2**, 181–184, doi:10.1038/ngeo437.
- Charlson, R. J., J. Langner, H. Rodhe, C. B. Leovy, and S. G. Warren, 1991: Perturbation of the northern hemisphere radiative balance by backscattering from anthropogenic sulfate aerosols. *Tellus*, **43A**, 152–163, doi:10.1034/j.1600-0870.1991.00013.x.
- Chung, C. E., and V. Ramanathan, 2006: Weakening of north Indian SST gradients and the monsoon rainfall in India and the Sahel. *J. Climate*, **19**, 2036–2045.
- Chylek, P., and J. Wong, 1995: Effect of absorbing aerosols on global radiation budget. *Geophys. Res. Lett.*, **22**, 929–931.
- Coakley, J. A., and R. D. Cess, 1985: Response of the NCAR Community Climate Model to the radiative forcing by the naturally occurring tropospheric aerosol. *J. Atmos. Sci.*, **42**, 1677–1692.
- Collier, J., and G. Zhang, 2009: Aerosol direct forcing of the summer Indian monsoon as simulated by the NCAR CAM3. *Climate Dyn.*, **32**, 313–332, doi:10.1007/s00382-008-0464-9.
- Denman, K., and Coauthors, 2007: Couplings between changes in the climate system and biogeochemistry. *Climate Change 2007: The Physical Science Basis*. S. Solomon et al., Eds., Cambridge University Press, 499–587.
- Emmons, L. K., and Coauthors, 2010: Description and evaluation of the Model for Ozone and Related Chemical Tracers, version 4 (MOZART-4). *Geosci. Model Dev.*, **3**, 43–67, doi:10.5194/gmd-3-43-2010.
- Forster, P., and Coauthors, 2007: Changes in atmospheric constituents and in radiative forcing. *Climate Change 2007: The Physical Science Basis*. S. Solomon et al., Eds., Cambridge University Press, 129–234.

- Hansen, J., M. Sato, and R. Ruedy, 1997: Radiative forcing and climate response. *J. Geophys. Res.*, **102** (D6), 6831–6864.
- Haywood, J. M., and K. P. Shine, 1995: The effect of anthropogenic sulfate and soot aerosol on the clear sky planetary radiation budget. *Geophys. Res. Lett.*, **22**, 603–606.
- , S. R. Osborne, P. N. Francis, A. Keil, P. Formenti, M. O. Andreae, and P. H. Kaye, 2003: The mean physical and optical properties of regional haze dominated by biomass burning aerosol measured from the C-130 aircraft during SAFARI 2000. *J. Geophys. Res.*, **108**, 8473, doi:10.1029/2002JD002226.
- , —, and S. J. Abel, 2004: The effect of overlying absorbing aerosol layers on remote sensing retrievals of cloud effective radius and cloud optical depth. *Quart. J. Roy. Meteor. Soc.*, **130**, 779–800, doi:10.1256/qj.03.100.
- Huang, J., A. Adams, C. Wang, and C. Zhang, 2009a: Black carbon and West African monsoon precipitation: Observations and simulations. *Ann. Geophys.*, **27**, 4171–4181, doi:10.5194/angeo-27-4171-2009.
- , C. Zhang, and J. M. Prospero, 2009b: African dust outbreaks: A satellite perspective of temporal and spatial variability over the tropical Atlantic Ocean. *J. Geophys. Res.*, **115**, D05202, doi:10.1029/2009JD012516.
- Huneus, N., and Coauthors, 2011: Global dust model intercomparison in AeroCom phase I. *Atmos. Chem. Phys.*, **11**, 7781–7816, doi:10.5194/acp-11-7781-2011.
- Johnson, B. T., K. P. Shine, and P. M. Forster, 2004: The semi-direct aerosol effect: Impact of absorbing aerosols on marine stratocumulus. *Quart. J. Roy. Meteor. Soc.*, **130**, 1407–1422, doi:10.1256/qj.03.61.
- Junker, C., and C. Liousse, 2008: A global emission inventory of carbonaceous aerosol from historic records of fossil fuel and biofuel consumption for the period 1860–1997. *Atmos. Chem. Phys.*, **8**, 1195–1207, doi:10.5194/acp-8-1195-2008.
- Kasischke, E. S., and J. E. Penner, 2004: Improving global estimates of atmospheric emissions from biomass burning. *J. Geophys. Res.*, **109**, D14S01, doi:10.1029/2004JD004972.
- Kaufman, Y., and Coauthors, 2005: A critical examination of the residual cloud contamination and diurnal sampling effects on MODIS estimates of aerosol over ocean. *IEEE Trans. Geosci. Remote Sens.*, **43**, 2886–2897, doi:10.1109/TGRS.2005.858430.
- Koch, D., and Coauthors, 2009: Evaluation of black carbon estimations in global aerosol models. *Atmos. Chem. Phys.*, **9**, 9001–9026, doi:10.5194/acp-9-9001-2009.
- Koren, I., Y. J. Kaufman, L. A. Remer, and J. V. Martins, 2004: Measurement of the effect of Amazon smoke on inhibition of cloud formation. *Science*, **303**, 1342–1345.
- Lamarque, J.-F., J. T. Kiehl, P. G. Hess, W. D. Collins, L. K. Emmons, P. Ginoux, C. Luo, and X. X. Tie, 2005: Response of a coupled chemistry–climate model to changes in aerosol emissions: Global impact on the hydrological cycle and the tropospheric burdens of OH, ozone, and NO<sub>x</sub>. *Geophys. Res. Lett.*, **32**, L16809, doi:10.1029/2005GL023419.
- , and Coauthors, 2010: Historical (1850–2000) gridded anthropogenic and biomass burning emissions of reactive gases and aerosols: Methodology and application. *Atmos. Chem. Phys.*, **10**, 7017–7039, doi:10.5194/acp-10-7017-2010.
- Lau, K., M. Kim, and K. Kim, 2006: Asian summer monsoon anomalies induced by aerosol direct forcing: The role of the Tibetan Plateau. *Climate Dyn.*, **26**, 855–864, doi:10.1007/s00382-006-0114-z.
- Mahajan, S., R. Saravanan, and P. Chang, 2009: The role of the wind–evaporation–sea surface temperature (WES) feedback in air–sea coupled tropical variability. *Atmos. Res.*, **94**, 19–36.
- , —, and —, 2010: Free and forced variability of the tropical Atlantic Ocean: Role of the wind–evaporation–sea surface temperature feedback. *J. Climate*, **23**, 5958–5977.
- Mahowald, N. M., J.-F. Lamarque, X. X. Tie, and E. Wolff, 2006a: Sea-salt aerosol response to climate change: Last glacial maximum, preindustrial, and doubled carbon dioxide climates. *J. Geophys. Res.*, **111**, D05303, doi:10.1029/2005JD006459.
- , D. R. Muhs, S. Levis, P. J. Rasch, M. Yoshioka, C. S. Zender, and C. Luo, 2006b: Change in atmospheric mineral aerosols in response to climate: Last glacial period, preindustrial, modern, and doubled carbon dioxide climates. *J. Geophys. Res.*, **111**, D10202, doi:10.1029/2005JD006653.
- , and Coauthors, 2010: Observed 20th century desert dust variability: Impact on climate and biogeochemistry. *Atmos. Chem. Phys.*, **10**, 875–10 893, doi:10.5194/acp-10-10875-2010.
- Matichuk, R. I., P. R. Colarco, J. A. Smith, and O. B. Toon, 2007: Modeling the transport and optical properties of smoke aerosols from African savanna fires during the Southern African Regional Science Initiative Campaign (SAFARI 2000). *J. Geophys. Res.*, **112**, D08203, doi:10.1029/2006JD007528.
- Neale, R. B., and Coauthors, 2010: Description of the NCAR Community Atmosphere Model (CAM4). NCAR Tech. Rep. NCAR/TN-485+STR, 194 pp.
- Philander, S. G. H., D. Gu, G. Lambert, T. Li, D. Halpern, N. C. Lau, and R. C. Pacanowski, 1996: Why the ITCZ is mostly north of the equator. *J. Climate*, **9**, 2958–2972.
- Pöschl, U., and Coauthors, 2010: Rainforest aerosols as biogenic nuclei of clouds and precipitation in the Amazon. *Science*, **329**, 1513–1516.
- Prospero, J. M., and T. Carlson, 1972: Vertical and areal distribution of Saharan dust over the western equatorial North Atlantic Ocean. *J. Geophys. Res.*, **77**, 5255–5265.
- , and P. J. Lamb, 2003: African droughts and dust transport to the Caribbean: Climate change implications. *Science*, **302**, 1024–1027.
- Quaas, J., and Coauthors, 2009: Aerosol indirect effects—General circulation model intercomparison and evaluation with satellite data. *Atmos. Chem. Phys.*, **9**, 8697–8717, doi:10.5194/acp-9-8697-2009.
- Ramanathan, V., and Coauthors, 2001: Indian Ocean experiment: An integrated analysis of the climate forcing and effects of the great Indo-Asian haze. *J. Geophys. Res.*, **106** (D22), 28 371–28 398.
- , and Coauthors, 2005: Atmospheric brown clouds: Impacts on South Asian climate and hydrological cycle. *Proc. Natl. Acad. Sci. USA*, **102**, 5326–5333.
- Rayner, N. A., P. Brohan, D. E. Parker, C. K. Folland, J. J. Kennedy, M. Vanicek, T. J. Ansell, and S. F. B. Tett, 2006: Improved analyses of changes and uncertainties in sea surface temperature measured in situ since the mid-nineteenth century: The HadSST2 dataset. *J. Climate*, **19**, 446–469.
- Remer, L. A., and Coauthors, 2005: The MODIS aerosol algorithm, products, and validation. *J. Atmos. Sci.*, **62**, 947–973.
- Rosenfeld, D., 2000: Suppression of rain and snow by urban and industrial air pollution. *Science*, **287**, 1793–1796.
- Sakaeda, N., R. Wood, and P. J. Rasch, 2011: Direct and semidirect aerosol effects of southern African biomass burning aerosol. *J. Geophys. Res.*, **116**, D12205, doi:10.1029/2010JD015540.

- Saravanan, R., and P. Chang, 2004: Thermodynamic coupling and predictability of tropical sea surface temperature. *Earth Climate: The Ocean–Atmosphere Interaction, Geophys. Monogr.*, Vol. 147, Amer. Geophys. Union, 171–180.
- Satheesh, S. K., and V. Ramanathan, 2000: Large differences in tropical aerosol forcing at the top of the atmosphere and Earth's surface. *Nature*, **405**, 60–63, doi:10.1038/35011039.
- Schultz, M. G., and Coauthors, 2008: Global wildland fire emissions from 1960 to 2000. *Global Biogeochem. Cycles*, **22**, GB2002, doi:10.1029/2007GB003031.
- Smith, S. J., H. Pitcher, and T. Wigley, 2001: Global and regional anthropogenic sulfur dioxide emissions. *Global Planet. Change*, **29**, 99–119, doi:10.1016/S0921-8181(00)00057-6.
- , J. van Aardenne, Z. Klimont, R. J. Andres, A. Volke, and S. Delgado Arias, 2011: Anthropogenic sulfur dioxide emissions: 1850–2005. *Atmos. Chem. Phys.*, **11**, 1101–1116, doi:10.5194/acp-11-1101-2011.
- Tie, X., G. Brasseur, L. Emmons, L. Horowitz, and D. Kinnison, 2001: Effects of aerosols on tropospheric oxidants: A global model study. *J. Geophys. Res.*, **106** (D19), 22 931–22 964.
- , and Coauthors, 2005: Assessment of the global impact of aerosols on tropospheric oxidants. *J. Geophys. Res.*, **110**, D03204, doi:10.1029/2004JD005359.
- Twomey, S., 1977: The influence of pollution on the shortwave albedo of clouds. *J. Atmos. Sci.*, **34**, 1149–1152.
- Wilcox, E. M., 2010: Stratocumulus cloud thickening beneath layers of absorbing smoke aerosol. *Atmos. Chem. Phys.*, **10**, 11 769–11 777, doi:10.5194/acp-10-11769-2010.
- Williamson, D. L., 2008: Equivalent finite volume and Eulerian spectral transform horizontal resolutions established from aqua-planet simulations. *Tellus*, **60A**, 839–847, doi:10.1111/j.1600-0870.2008.00340.x.
- Wood, R., and D. L. Hartmann, 2006: Spatial variability of liquid water path in marine low cloud: The importance of mesoscale cellular convection. *J. Climate*, **19**, 1748–1764.
- Xie, S.-P., and J. Carton, 2004: Tropical Atlantic variability: Patterns, mechanisms, and impacts. *Earth Climate: The Ocean–Atmosphere Interaction, Geophys. Monogr.*, Vol. 147, Amer. Geophys. Union, 121–142.
- Yoshioka, M., N. M. Mahowald, A. J. Conley, W. D. Collins, D. W. Fillmore, C. S. Zender, and D. B. Coleman, 2007: Impact of desert dust radiative forcing on Sahel precipitation: Relative importance of dust compared to sea surface temperature variations, vegetation changes, and greenhouse gas warming. *J. Climate*, **20**, 1445–1467.
- Yu, H., and Coauthors, 2006: A review of measurement-based assessments of the aerosol direct radiative effect and forcing. *Atmos. Chem. Phys.*, **6**, 613–666, doi:10.5194/acp-6-613-2006.
- Zender, C. S., H. Bian, and D. Newman, 2003: Mineral dust entrainment and deposition (DEAD) model: Description and 1990s dust climatology. *J. Geophys. Res.*, **108**, 4416, doi:10.1029/2002JD002775.